Final Technical Report

Testing Recurrence Models for the southernmost San Andreas Fault by Developing a New Paleoseismic Site at Durmid, Salton Trough: Collaborative Research with SDSU and USGS

USGS NEHRP Award No. G 21AP10005

Thomas Rockwell
William Buckley
Patrick Williams
Allen Gontz
Department of Geological Sciences
San Diego State University
5500 Campanile Dr.
San Diego, CA 92182-1020
P: (619) 594-4441, trockwell@mail.sdsu.edu

In Collaboration with
Kate Scharer
US Geological Survey
Pasadena, CA
(626) 583-7240 kscharer@usgs.gov

And
Paula

Abstract

We conducted a paleoseismic and geomorphic study along the southernmost San Andreas fault to better constrain the timing of past earthquakes and develop information on displacement in past earthquakes. Low-altitude UAV (drone) imagery was flown along four sections of the fault between Durmid and Indio Hills from which we produced high-resolution DEMs, orthomosaics, hillshades, topographic maps and slope maps. Offset channels, rills, alluvial bars and other geomorphic features were identified in the imagery and measured to resolve lateral displacement, and all offsets were checked and measured in the field. From these data, we construct slip distribution from Durmid to the Indio Hills for the past several earthquakes. The average of the past four interpreted earthquakes is ~3.3 m, and ~3.7 m for the past six events, indicating that at least one earlier earthquake sustained higher than average displacement. At the proposed trench site at Ferrum near Durmid Hill, a small pull-apart basin from a double releasing bend, we applied two geophysical tools, ground penetrating radar (GPR) and electrical resistivity tomography (ERT), to image the subsurface at the site. We then excavated two trenches to about 2 m depth to explore the age of sediments and to expose the fault zone. These trenches exposed only sediments from the most recent highstand of Lake Cahuilla, indicating a very high rate of sedimentation. Although the site may contain an excellent paleoseismic record, we did not have permission to excavate a massive, deep benched trench, which would have been required to extend the record back to the target of about 900 CE. Hence, this site was abandoned and we focused on recovering the earthquake record from Salt Creek, which is still in progress.

Introduction and Background

The focus of this project was to develop a new paleoseismic site along the southernmost San Andreas fault (SAF) as much of the logging and primary data from the Salt Creek site was believed to be lost. The earthquake history of the southernmost 150 km of the San Andreas fault is mostly determined from sites in the Coachella Valley from Indio Hills and to the northwest (Figure 1), leaving the southern 75 km uncharted. There are many unresolved questions relating to the fault's rupture history and the relationship between earthquake events and lake filling events associated with ancient Lake Cahuilla, which episodically has filled the broader Salton Sea basin (Rockwell et al., 2022). One of the goals of this project was to develop a new paleoseismic site along the southernmost San Andreas fault at Durmid to resolve outstanding questions on its past earthquake history. The fault had a published average recurrence interval of large earthquakes of 150-180 years between about CE 950 and 1726 (Philibosian et al., 2011) but has been quiet now for nearly 300 years (Rockwell et al., 2018). More information is needed to resolve whether the fault is really "overdue" for a large earthquake, which will have devastating effects on large areas of southern California, or whether this long open-interval is the result of the interplay between earthquakes and filling events of ancient Lake Cahuilla, as the last full lake was also 300 years ago and the two most recent surface ruptures occurred when the lake was full.

The Durmid site at Ferrum (an old railroad turn-around point for a mining company) is ideal because it lies 56 m below the elevation of the shoreline of Lake Cahuilla, so it can provide information on the relative timing of earthquakes and lakes that are, in some cases, ambiguous at

Figure 1. *Paleoseismic and slip rate sites along the southernmost San Andreas fault in the Salton Trough. Note the lack of published data along the southernmost 75 km of fault.*

or near the shoreline. The site is a small 100-m scale pull-apart basin resulting from a double releasing bend in the fault, and earthquakes produce an uphill-facing scarp that is ideal for trapping lacustrine and alluvial fan sediments (Figure 2). The current earthquake history of the southern San Andreas fault only extends back about a thousand years, as that is the period during which there were six full fillings of Lake Cahuilla. Prior to about CE 950, there was an extended dry period back to about 2,000 years ago (Rockwell et al., 2022) and there are no data on earthquakes for this period. The Durmid site has the potential to confirm the earthquake record back to CE 950, resolve some questions about the current record, and extend the record back to 2,000 or more years because the uphill-facing scarp has the potential to trap fluvial sediments that capture the earthquake history through the dry period. As discussed below, however, the sedimentation rate turned out to be extremely high, which means to achieve this goal will require very deep trenches and that was not possible for this study, both due to the lack of sufficient funds, and more importantly because our permission was limited to ~4 m deep trenches.

A second component of the project was to refine estimates of displacement in past earthquakes by adding to the catalogue of small offset rills, stream channels, alluvial bars and other linear geomorphic features that can record displacement. This aspect was accomplished by detailed surface mapping in the vicinity from Durmid Hill to Indio Hills. We flew UAV (drone) surveys along four sections of the fault for detailed mapping in areas that looked most promising for small displacements. We combine the observations from this mapping with prior work (Blanton et al., 2020) and unpublished field mapping by Pat Williams to construct slip distribution curves for the past several earthquakes. The results of this work have been submitted to the Bulletin of the Seismological Society of America. One aspect is noteworthy: this section of the fault creeps at about 3 mm/yr (about 15-20% of the total slip rate) based on InSAR and

previous work (Lindsey et al., 2014; Blanton et al., 2020), and recessional shorelines are offset about 80-100 cm on Durmid Hill, confirming that this rate has not changed significantly since the lake dried up starting about 290 years ago.

The Durmid Hill – Ferrum Site

The Durmid paleoseismic site lies on the flanks of the Durmid anticlinorium where the fault makes a 120-m-wide double releasing bend or step resulting in an uphill-facing scarp that has trapped Holocene sediments (Figure 2). The folded Pleistocene bedrock is exposed at the surface on the southwest side of the fault as well as on the northeast side to the north and south of the double bend, but in the area of the bend/step, sediment is being trapped on the northeast side of the fault.

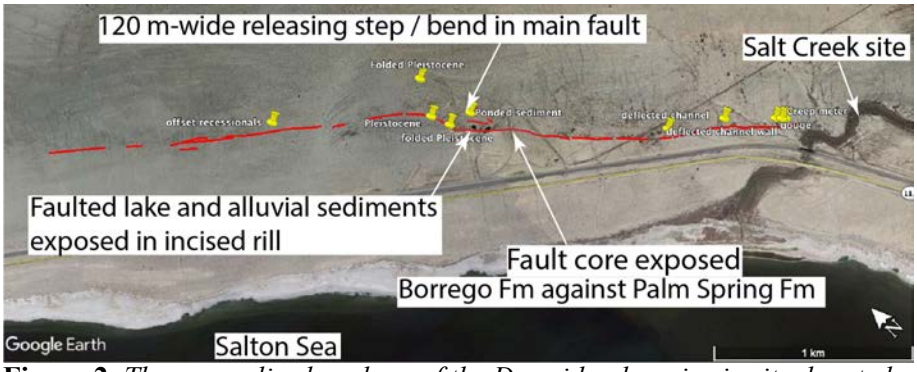

Figure 2. *The generalized geology of the Durmid paleoseismic site, located about 2 km northwest from Salt Creek. The San Andreas fault is well-defined by offset shorelines and the main fault core is exposed in several locations in rills and rail line exposures. The 120 m-wide step produces down-to-the-north vertical slip in the area of the step, trapping Holocene sediment behind the uphill-facing scarp. The sediment is composed of well-bedded lacustrine and alluvial fan deposits that contain charcoal and shell.*

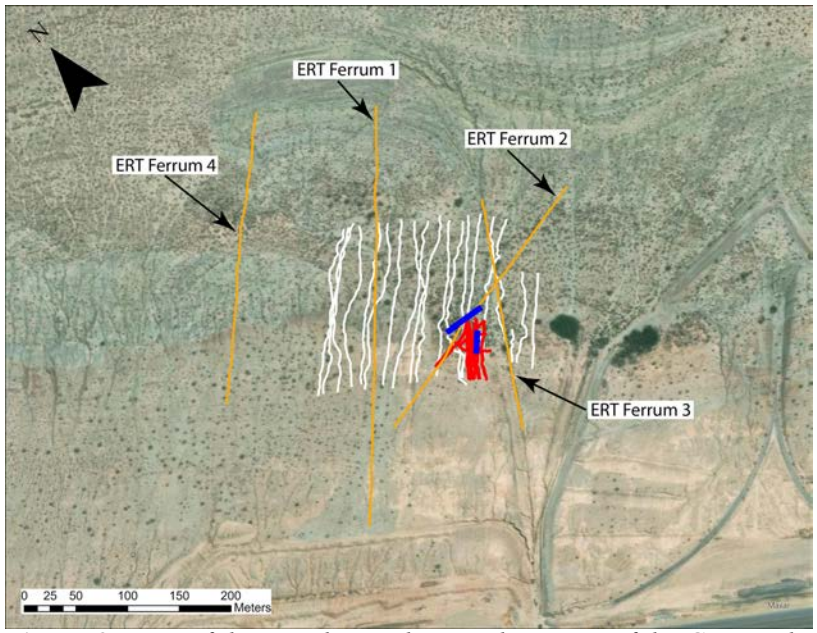

Figure 3. *Map of the trench site showing locations of the GPR and ERT lines. GPR lines white and red, ERT in orange, trenches in blue.*

Geophysical Surveys

We conducted ground penetrating radar (GPR) and electromagnetic resistivity tomography (ERT) surveys in the proposed trench site to investigate subsurface conditions prior to trenching, as well as search for locations of faults. Figure 3 is a map of the site showing the geophysical lines along with the location of the two trenches excavated for this project. The broader-scope GPR lines are shown in white, whereas a detailed survey specifically over the area we wanted to trench is shown red. The trenches are shown in blue. The GPR lines imaged the subsurface and potentially identified some fault strands in the upper 2-3 m,

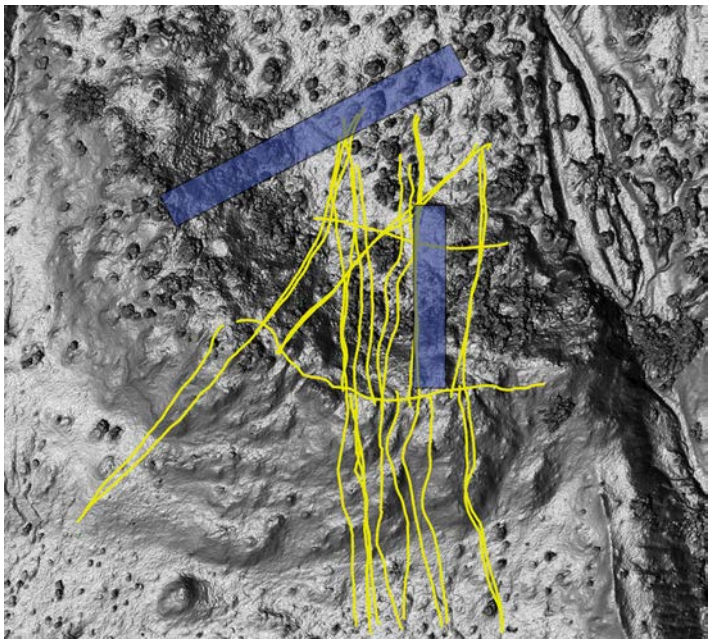

Figure 4. *Detail of GPR survey in area of trenches, which are shown in blue.*

but the data were not compelling. Figure 4 shows the detailed GPR lines in the area of proposed trenching. Figures 5 and 6 show examples of the GPR data along the trench alignment. A fault was interpreted in line DAT0392 (Figure 5) at over a meter depth, which was promising. Figure 6 shows a nearby, parallel line, DAT0390, to the south within the footprint of trench 1. The interpreted fault lies west of the fault interpreted in line DAT0392 by at least 2 meters suggesting that fault strikes to the NE. This relationship became more clear when we opened trench 1 and found the fault on the north wall, as expected, but the fault was not exposed on the south wall directly across from the north wall fault. This is easily explained if the fault strikes northeast, with the equivalent fault being in the older dune deposits exposed near the western end of the trench, as discussed below.

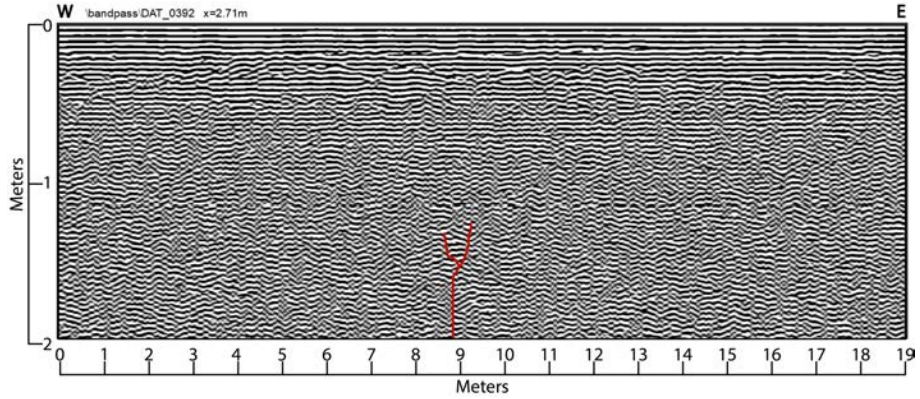

Figure 5. *Interpreted GPR line DAT0392 from the 450 mhz survey adjacent to the north wall of trench 1. A fault was interpreted near the center of the line.*

The ERT transects, shown in orange in Figure 3, provided a clear picture of subsurface conditions over a broader area. A total of four survey lines were employed to collect subsurface information in a corridor measuring approximately 270 m across the surficial expression of the fault. Survey lines ranged between 235 and 395 m in length with electrode spacing set at 5 m for most lines. We used 2 m spacing for one survey line which covered our area of interest for paleoseismic trenching. All survey lines were orientated

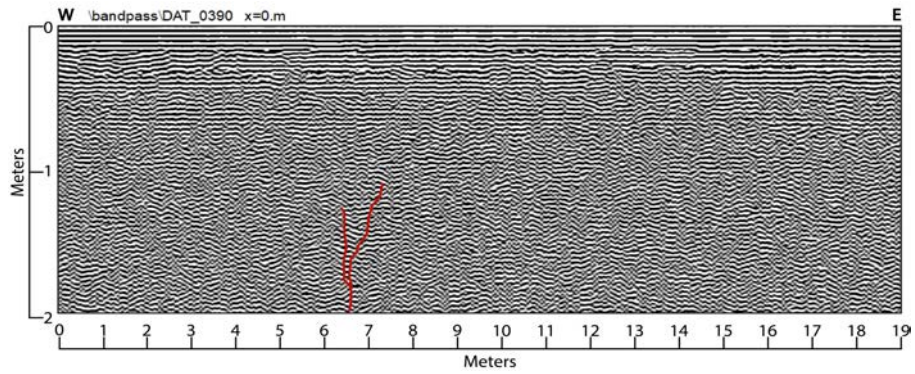

Figure 6. *Interpreted GPR line DAT0390 from the 450 mhz survey close to the centerline of trench 1. A fault was interpreted a little west of the fault from line DAT0392 suggesting a NE strike.*

perpendicular to the surficial expression of the fault trace. Figures 7 - 10 display the results of ERT transects Ferrum 1 through 4.

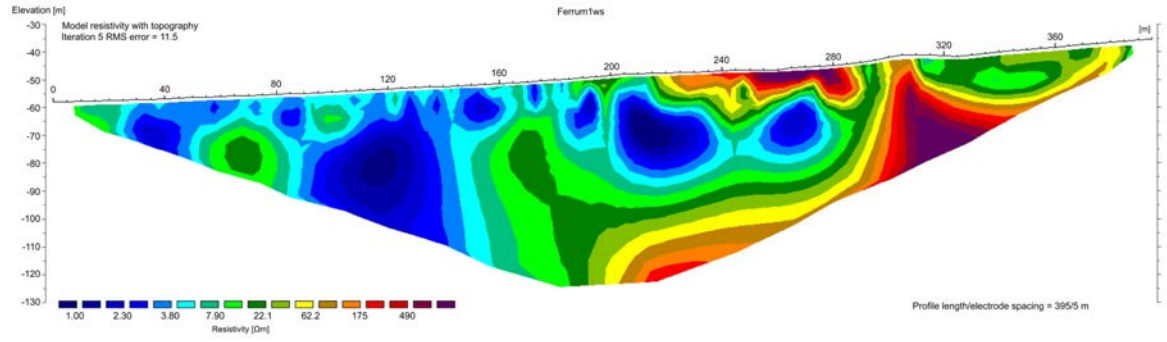

Figure 7. *Interpreted ERT line Ferrum 1. The main strand of the San Andreas fault is clear at about station 140. Surficial outcrops of bedrock are also clearly expressed to the NE near station 300.*

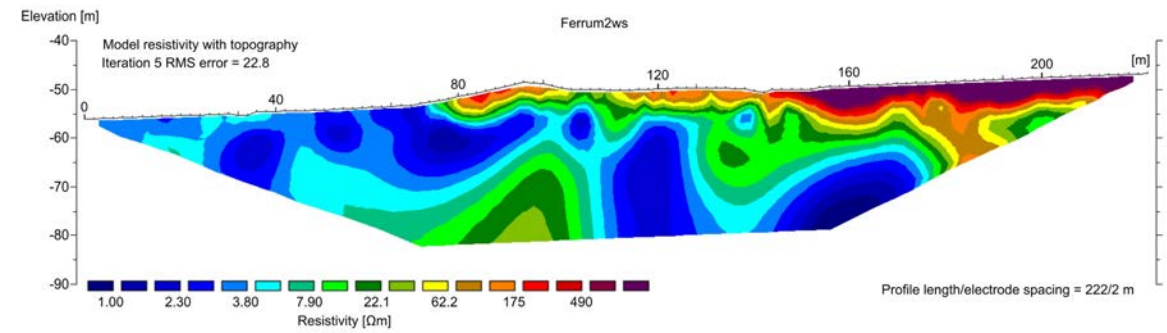

Figure 8. *ERT line Ferrum 2 was ran through the trench site at an angle. The fault zone is apparently more complex in this area.*

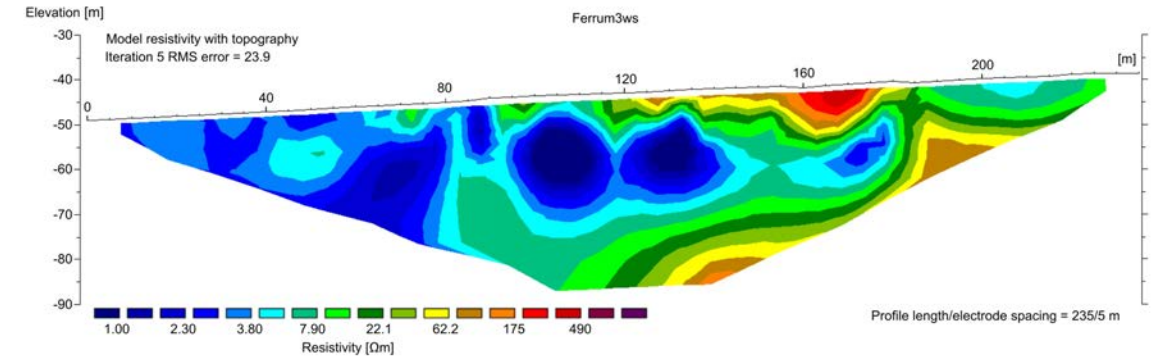

Figure 9. *ERT line Ferrum 3 lies south of the trench, and again, the main fault is well-expressed but there appears to be some complexity in faulting but the bedrock signature is clearly different from that of alluvium.*

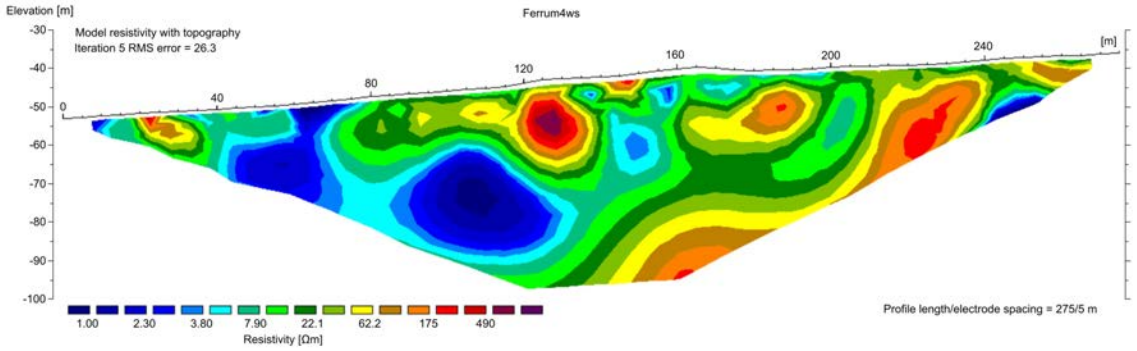

Figure 10. *ERT line Ferrum 4 was sited north of the double releasing bend where the surface trace of the fault was relatively simple with the main strand at about station140. A secondary strand, which is expressed at the surface in the geomorphology, is present at about station 60-65.*

Data from the ERT survey provide evidence for complex faulting along the sSAF at Ferrum. The main strand was verified in our models along with several minor fault splays. Surficial expressions of the minor splays are present near the main strand of the fault; however, these strands become buried to the northwest.

Trench Results

We excavated two trenches across the area that looked most promising from the geophysical surveys, as shown on Figure 2. Trench 1 exposed highly sheared sand dune deposits at the southwest end of the trenches (Figures 11-13 for the north face, and Figures 14 and 15 for the south face). The fine-grained, well-sorted sand of the dune complex interfingered with lacustrine silt and sand deposits to the northeast of the dune complex in the area of the sag depression. The lacustrine section expressed four distinct packages of lacustrine deposits interbedded with well-sorted fine-grained sand that we interpreted were derived from the dune. At the time of trench logging, we were perplexed because we found evidence for only a single event in the north face of trench 1 whereas we initially interpreted up to four lake phases. Radiocarbon dating of gastropod shells from the lowest to highest stratigraphic units (Table 1) revealed that the entire section dates to only the last highstand of Lake Cahuilla at ca 1732 CE as the shell ages ranged from 545 to 7,840 radiocarbon years B.P., with shell ages of 545 to 580 from unit 30 down through unit 80. Applying a ΔR correction of zero calibrates the youngest shell ages to the period of 1697-1736 CE, consistent with Lake A of Rockwell et al. (2018, 2022).

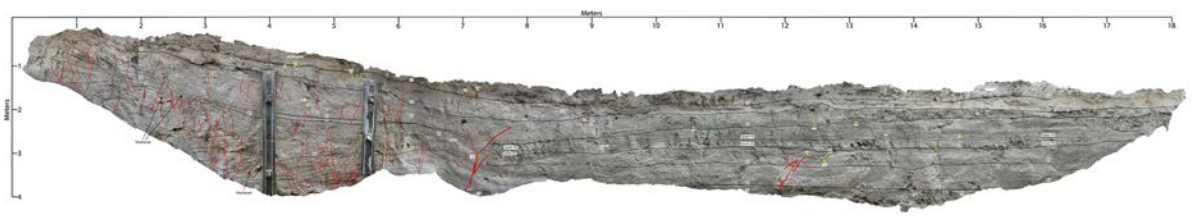

Figure 11. *Mosaic and log of the north wall of T1. Details of the fault imaged in the GPR and the fault zone in the dune complex are shown in Figures 12 and 13.*

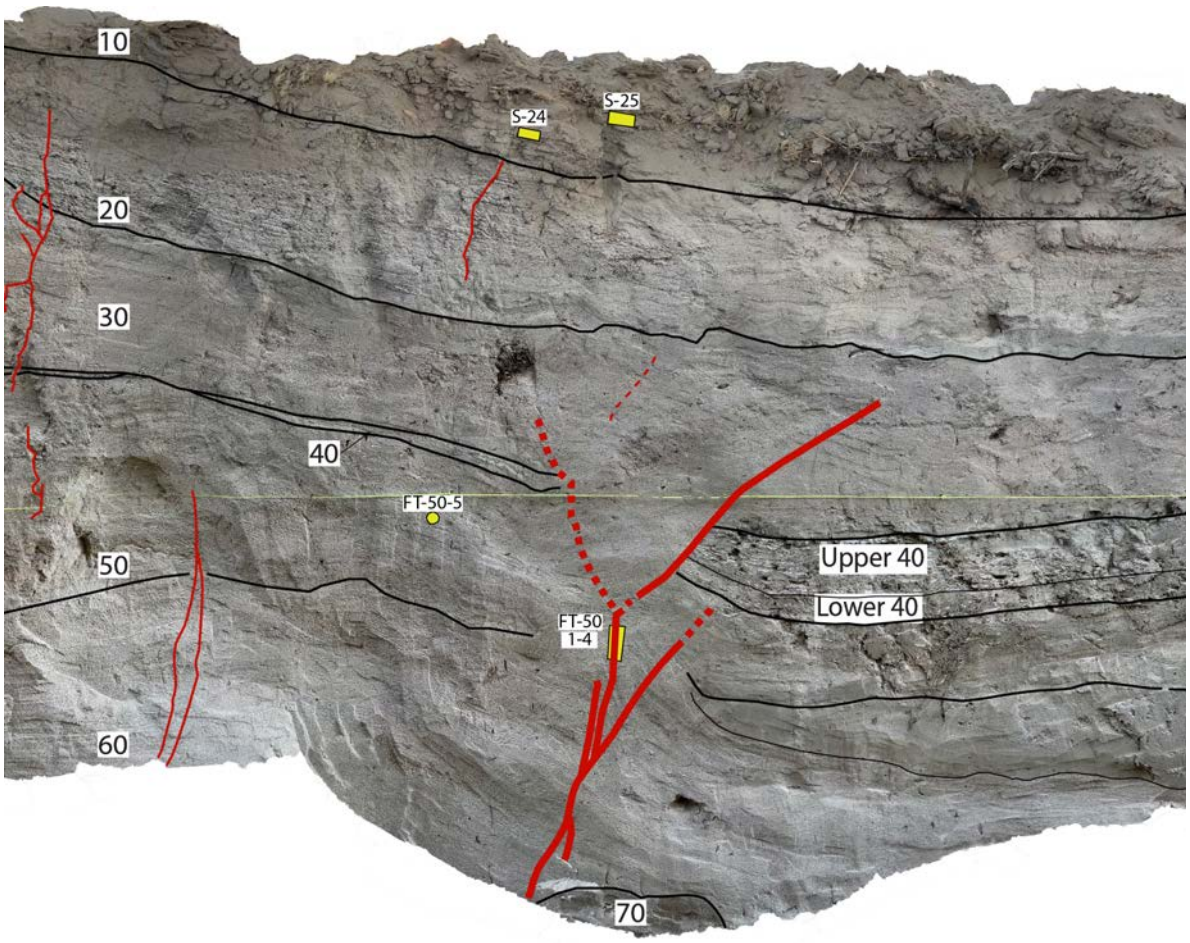

Figure 12. *Detail of the fault in the north wall of trench 1 that was imaged by GPR. There is only evidence here for a single event that occurred during the most recent lake..*

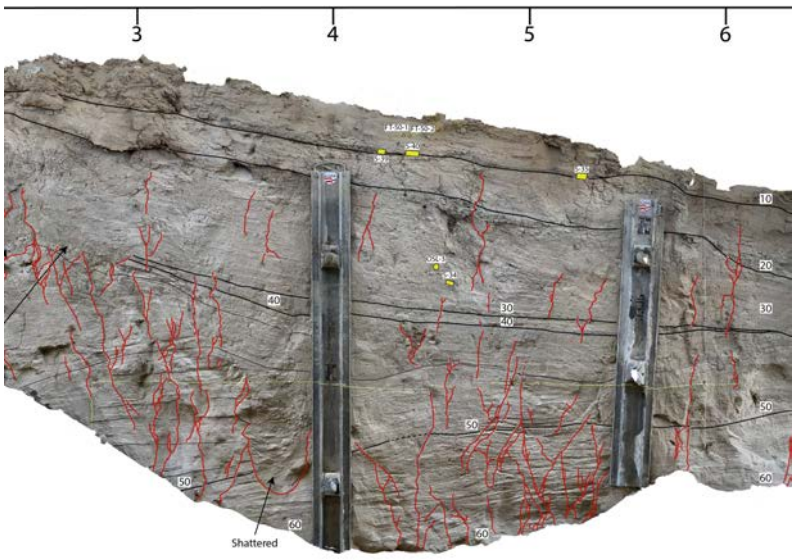

Figure 13. *Detail of the highly shear sand in the dune complex that overlies the long-term main fault. Faulting is highly distributed and there are no distinct event horizons.*

Radiocarbon Dates for Ferrum Trench Samples								
UCIAMS No.	Stratigraphic Unit	Sample Name	Fraction Modern	±	$D^{14}C$ (‰)	±	^{14}C age (BP)	±
250317	10	FT1 S21 Tryonia	0.9015	0.0016	-98.5	1.6	835	15
250318	10	FT1 S21 Gastropod	0.8507	0.0017	-149.3	1.7	1300	20
250320	10	FT1 S25 Tryonia	0.8972	0.0017	-102.8	1.7	870	20
250316	20	FT1 S18 baby Physa	0.8398	0.0015	-160.2	1.5	1405	15
250319	20	FT1 S22 Tryonia	0.7263	0.0016	-273.7	1.6	2570	20
250322	20	FT1 S27 Tryonia	0.8985	0.0017	-101.5	1.7	860	20
250321	30	FT1 S26 Tryonia	0.9184	0.0016	-81.6	1.6	685	15
250323	30	FT1 S28 Tryonia	0.8890	0.0017	-111.0	1.7	945	20
250328	30	FT1 S33 Tryonia	0.8871	0.0019	-112.9	1.9	960	20
250329	30	FT1 S33 baby Physa	0.8612	0.0015	-138.8	1.5	1200	15
250330	30	FT1 S34 baby Physa	0.8668	0.0015	-133.2	1.5	1150	15
250304	30/40	FT1 S4 Physa	0.9343	0.0015	-65.7	1.5	545	15
250305	40	FT1 S7 Physa	0.7198	0.0013	-280.2	1.3	2640	15
250306	40	FT1 S7 Tryonia	0.8968	0.0014	-103.2	1.4	875	15
250327	40	FT1 S32 Tryonia	0.9070	0.0017	-93.0	1.7	785	20
250334	40	FT1 S46 Physa	0.8778	0.0015	-122.2	1.5	1045	15
250335	40	FT1 S46 Tryonia	0.9212	0.0016	-78.8	1.6	660	15
250303	50	FT1 S2 Physa	0.7232	0.0013	-276.8	1.3	2605	15
250307	50	FT1 S10 Physa	0.8161	0.0013	-183.9	1.3	1630	15
250308	50	FT1 S10 Tryonia	0.8951	0.0015	-104.9	1.5	890	15
250309	50	FT1 S11 Tryonia	0.9110	0.0017	-89.0	1.7	750	20
250310	50	FT1 S12 Tryonia	0.8816	0.0015	-118.4	1.5	1010	15
250333	50	FT1 S45 Physa	0.8453	0.0015	-154.7	1.5	1350	15
250311	60	FT1 S13 Physa	0.9317	0.0018	-68.3	1.8	570	20
250312	60	FT1 S13 Tryonia	0.8788	0.0016	-121.2	1.6	1040	15
250326	60	FT1 S31 Tryonia	0.9245	0.0018	-75.5	1.8	630	20
250332	60	FT1 S44 Tryonia	0.9249	0.0016	-75.1	1.6	625	15
250315	70	FT1 S15 Physa	0.3769	0.0008	-623.1	0.8	7840	20
250314	80	FT1 S14 Tryonia	0.9078	0.0016	-92.2	1.6	775	15
250331	80	FT1 S43 Tryonia	0.9212	0.0016	-78.8	1.6	660	15
250338	80	FT1 S47 Physa	0.9304	0.0016	-69.6	1.6	580	15
250339	80	FT1 S49 Physa	0.7737	0.0013	-226.3	1.3	2060	15
250340	N/A*	FT1 S50 Physa	0.8726	0.0015	-127.4	1.5	1095	15
250341	N/A*	FT1 S51 Physa	0.3864	0.0009	-613.6	0.9	7640	20
250342	N/A*	FT1 S51 Tryonia	0.8945	0.0016	-105.5	1.6	895	15

Table 1. *Radiocarbon dates on shells (Tryonia and Physa) from the Durmid Ferrum trench 1 (33.45820, -115.8559488). The dates ranged from 540 to 7,840 radiocarbon years, with no particular order, indicating extreme preservation and reworking of shell material. The youngest dates from unit 30 down through unit 80 are similar, and calibrate to the youngest filling of Lake Cahuilla, indicating that the entire section corresponds to Lake A. The samples list as N/A are from an arroyo exposure.*

The south face of trench 1 was perplexing at first as there was no correlative fault (Figure 14) across the trench from the well-expressed fault shown in the detail in Figure 12. In hind sight, the GPR indicated that the fault had a northeast strike through the area of trenching; if our interpretation is correct, the fault trends NE and would intersect the south face of the trench farther west, within the dune complex. Loose sands restricted our ability to extend the trench farther west to test this hypothesis. (Figure 15).

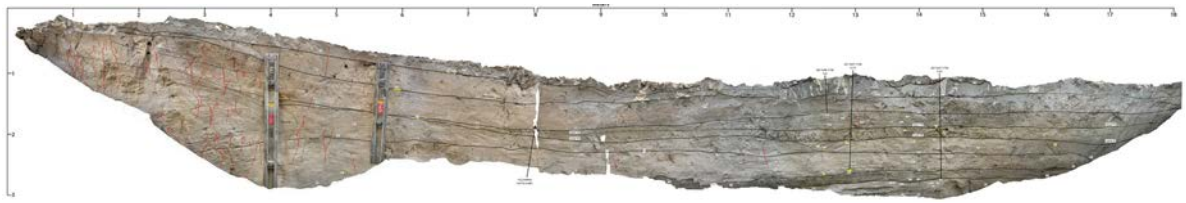

Figure 14. *Mosaic and log of the south face of trench 1 (flipped). No fault was identified northeast of the dune complex and shores, which are shown in the detail in Figure 15.*

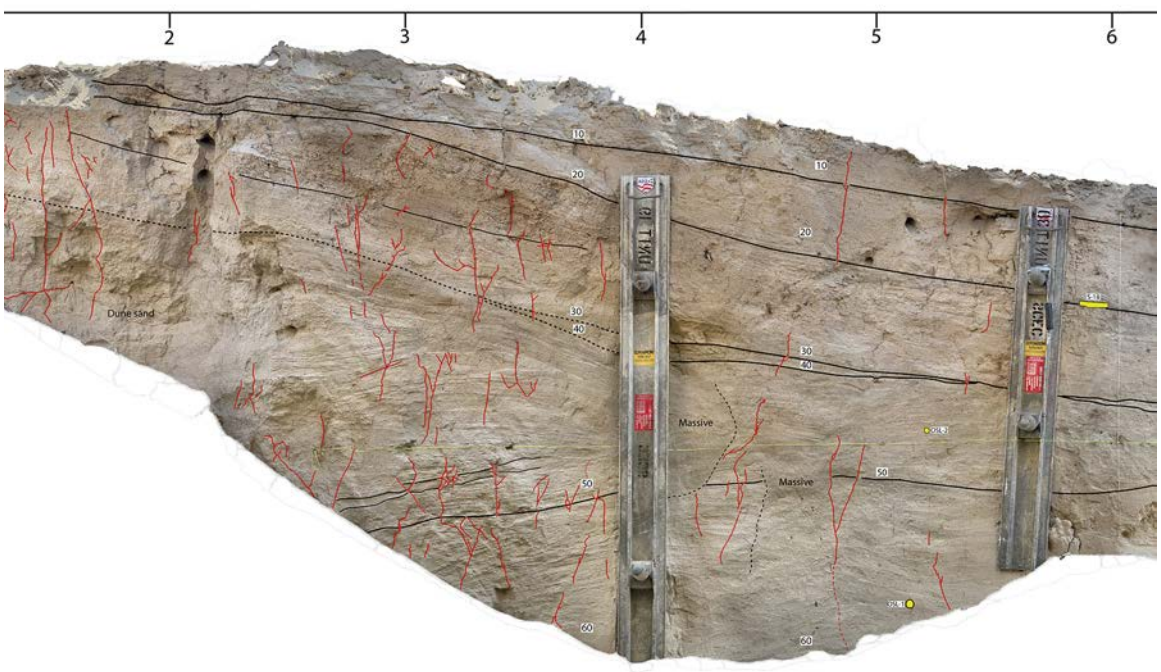

Figure 15. *Detail of the fault zone in the dune complex in the south face of trench 1 (flipped). Some fault strands reach the surface and probably represent the most recent event or surface creep.*

Trench 2 was excavated to the north of trench 1 (Figure 2) in an attempt to cross the projection of the fault in trench 1, but before we realized how northeasterly the fault strike was that transferred slip across the releasing bend. Trench 2 exposed similar stratigraphy as in trench 1, but with no exposed faults in the bedded section. The trench was photographed but not studied in detail.

In the end analysis, it appears that the sedimentation rate at the Ferrum site is very high, which should be good for paleoseismic studies. At that rate of sedimentation, it is conceivable that a trench would have been needed to be on the order of -12 m deep (2 meters per lake??) to match

the Coachella record of Philibosian et al. (2011) but we did not have permission to dig more than a slot trench for environmental reasons. We initially were going to extend to 3+ meters depth, but the sediments were very sandy and although we could have gone deeper with shoring (we shored the 2.5 m deep section in the sand dunes), we wanted to first understand the stratigraphy and sedimentation before deepening. As it turned out, a deep, benched trench would be quite wide and would not be acceptable for environmental reasons. Hence, we concluded this part of the field program. However, as presented later in this report, data that included logs and ^{14}C dates from the Salt Creek site were found by Dr. Patrick Williams during the course of our work; these were thought to have been lost. As some of the Salt Creek exposures from 2005 are still open, we refocused our paleoseismic efforts to recovering and completing the Salt Creek site. We present preliminary information and results of new dating after we present the geomorphic analysis completed for this project.

Geomorphic Analysis and Documentation of Slip per Event

This section is taken verbatim from a paper we recently submitted for review in BSSA entitled "Estimating slip along the southernmost ~80 km of the San Andreas fault by examining tectonically offset features", with W. Buckley, P. Williams, T. Rockwell, and A. Gontz as coauthors. We renumbered the figures such that they would be in sequence with the rest of this report.

ABSTRACT

We measured tectonically offset geomorphic features along approximately 80 km of the southernmost San Andreas Fault (sSAF) between Bombay Beach and Indio Hills in the Salton Trough to obtain a better estimate for slip distribution and slip-per-event for the past several large, surface rupturing earthquakes along this segment of the fault. In addition to gathering aerial imagery from previously published B4 light detection and ranging (LiDAR) and uncrewed aerial vehicle (UAV) imagery, we constructed new high-resolution orthomosaics and digital surface models (DSMs) generated from Structure-from-Motion-Multiview Stereo (SfM-MVS) techniques from UAV imagery at multiple localities along the San Andreas fault in the Salton Trough region of California, which include areas at Durmid Hill, Salt Creek, Ferrum, Mecca Hills, and Indio Hills. The aerial imagery, along with field mapping, were used to identify and measure a total of 146 offset features with lateral displacement measurements ranging between 2 to 23 m. Investigation of offset features suggests that the last several large, surface rupturing events produced average displacements of 3.1-4.4 m per event, with lower overall lateral slip values where multiple fault strands are present. Offset features displaying less than ~1 m of lateral displacement were not considered in our study as these features likely reflect modern creep and triggered slip events, which post-date the most recent surface rupturing event in ca 1726 AD.

INTRODUCTION

The southernmost San Andreas Fault (sSAF), extending from approximately Bombay Beach to Banning Pass in the Salton Trough (Fig. 16), has been the focus of several notable paleoseismic studies in the Coachella Valley and Salt Creek regions (Sieh and Williams, 1990; Fumal et al., 2002; Philibosian et al., 2011; Rockwell et al., 2018; Castillo et al., 2021), but information on displacement in the paleo- events is much more limited. Some displacement information was included in UCERF3 (Field et al., 2014; Field et al., 2015), and two recent studies in and near the Mecca Hills provide local information on displacement for the past few ruptures (Dingler et al., 2016; Blanton et al., 2020), but information on the distribution of slip in the past several earthquakes has not been constructed for the length of the southern SAF in the Salton Trough. In this paper, we present new information of the amount of displacement that has occurred in the past few large surface rupturing earthquakes from Bombay Beach northward to the Indio Hills based on offset geomorphic markers. This work builds on the previous studies in the Mecca Hills area (Blanton et al., 2020; Dingler et al., 2016) that suggest that the MRE produced 2.6 to 3.1 m of lateral displacement. We flew Uncrewed Aerial Vehicles (UAVs) to capture high-resolution imagery from which we produced Digital Surface Models (DSMs) and orthomosaics with centimeter-scale precision. We used these maps as a base for field work to resolve displacement on 146 offset features between the Indio Hills and Bombay Beach. We combine these new results with field measurements taken by one of the coauthors (Williams) 10-15 years ago to construct slip distribution for the past several earthquakes on the sSAF.

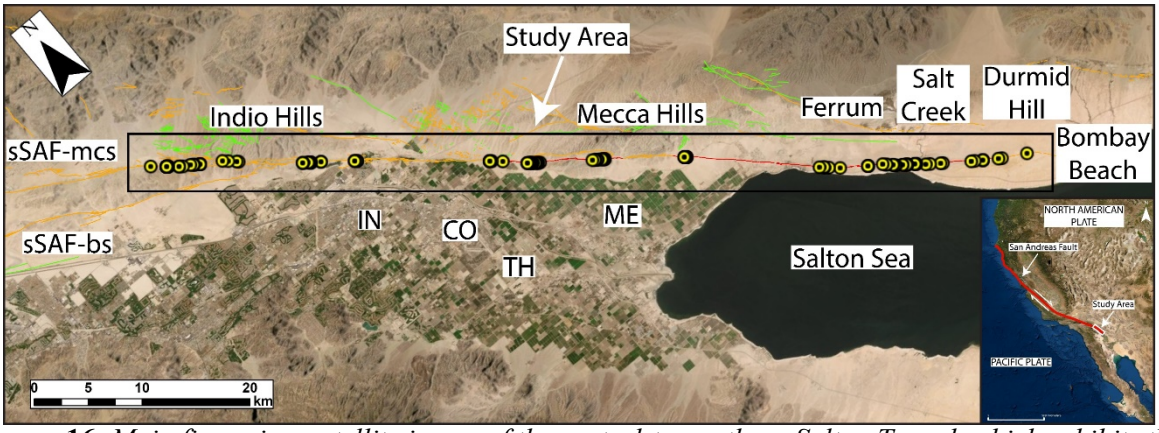

Figure 16. *Main figure is a satellite image of the central-to-northern Salton Trough which exhibits the location of our study area along ~80 km of the southernmost San Andreas Fault (sSAF), regional Quaternary faults (USGS and CGS, 2022) and lateral offset locations used in this presentation (yellow circles). Abbreviations: IN - Indio, CO - Coachella, TH - Thermal, ME - Mecca, SAF-mcs and bs – southernmost San Andreas Fault mission creek and banning strands. Inset figure (lower right) exhibits a map of North America in relation to our study site with the location of the San Andreas Fault (SAF) shown in red between the boundary of the North American and Pacific Plates.*

A complicating factor in estimating displacement in past earthquakes from geomorphic offset features is that the sSAF creeps in its upper 2-3 km at a rate of about 3 mm/yr (Lindsey et al., 2014; Sieh and Williams, 1990), resulting in additional uncertainty in slip measurements. As the majority of the fault is locked below the creeping zone, we believe that the creep is best interpreted as extended afterslip. If correct, then the additional slip from creep needs to be added to that which occurred co-seismically. The problem lies in not knowing the age of individual geomorphic features, such as small rills, channel margins, ridge noses, and alluvial bars, relative

to the age of the displacement events. Some creep may have accrued prior to a large earthquake if a particular feature was formed decades to a century prior to the earthquake. In this case, the offset may reflect both displacement from the earthquake and its associated afterslip as well as some displacement that may be attributed to the previous earthquake. In contrast, if a rill or other piercing line formed immediately prior to the earthquake, then the measured displacement may be smaller than the previous case. This could result in both larger uncertainty in estimating displacement in past events as well as an apparent variability in displacement laterally along the fault.

Blanton et al. (2020) showed that small displacements of about 20-23 and 50-51 cm are likely the result of incision during past hurricane and tropical storm strikes in 1939 and 1858, respectively. They also document that smaller storms that produced 3-6 cm of rain during the course of their study did not produce new incisions that would be used to measure displacement. This indicates that it is the very-large tropical storms that form during strong El Nino events that are likely to "reset" the landscape and produce geomorphic features that can be used to measure displacement in future earthquakes. Although the frequency of such events is not known, the historical record suggests that they occur about once per century. For the section of fault south of the Indio Hills, which has the shortest recurrence interval, the 3 mm/yr of creep in combination with the frequency of major storms imparts an uncertainty in slip estimation on the order of 30-50 cm.

Paleoseismic data, when combined with slip per event data, can be used as a cross check to test slip data against the fault slip rate as measured by geologic and geodetic methods. Paleoseismic studies conducted in Coachella Valley revealed a range of average recurrence intervals for surface-rupturing earthquakes in the past millennia; with about 180 years south of the Indio Hills (Philibosian et al., 2011, although that includes the current long open interval) to as much as 380-640 years north of the Indio Hills (Castillo et al., 2021). The most recent surface rupturing event south of the Indio Hills occurred around 1726 CE (Rockwell et al., 2018) which leaves a possibly atypically long 300-year open interval since the last large sSAF earthquake. To the north of Indio Hills, the most recent event is dated at 950 to 730 calibrated years BP, much earlier than to the south. We combine our new displacement data with paleoseismic records to verify a substantial set of displacement observations against known slip rate data.

REGIONAL SETTING

Geologic background

The Salton Trough is located in the Imperial and Coachella Valleys of southeastern, California, as well as the Mexicali Valley and Colorado River Delta in Mexico, and is a large, active tectonic pull-apart basin formed by the interaction of the SAF system and the northernmost portion of the East Pacific Rise known as the Gulf of California Rift Zone (GCRZ) (Fuis and Mooney, 1990). The SAF and GCRZ both terminate in close proximity to the Salton Sea, near the Brawley Seismic Zone, which connects the SAF with the Imperial Fault Zone (IFZ) to the south. As a result of this interaction, the Salton Trough has been subsiding; however, sedimentary deposits have filled the trough as quickly as it has been subsiding and in some areas the sediment has accumulated up to approximately 6,000 m in thickness (Younker et al., 1981). Sedimentary deposits filled the trough to a depth of as much as 6,000 meters as it subsides, indicating long-term subsidence of, ~1 mm/yr (Younker et al., 1981).

Regional mapping indicates that the Salton Trough is underlain by Holocene-aged surficial deposits and Pliocene-Pleistocene-aged sedimentary bedrock units (Brothers et al.,

2009). The surficial sediments consist of alluvial sand and gravel, deltaic and lacustrine silt and clay, as well as sand and gravelly bar deposits along the shoreline of ancient Lake Cahuilla and from a two-year flooding event between 1905 and 1907 CE (Ross, 2020) that resulted from a breached canal derived from spring flooding on the Colorado River, which consequently created the modern-day Salton Sea. The sedimentary bedrock units include the Palm Spring Formation (Tp), which consists of pink-gray laminated sandstone with interbedded clays and fossil hardwoods, and the Borrego Formation (Tbo), which consists of tan-gray lacustrine fossiliferous claystone.

Ancient Lake Cahuilla

During the late Holocene the Salton Trough experienced repeated filling and desiccation events as a result of cyclic diversions of the Colorado River (Waters, 1983; Rockwell et al., 2022). Filling events were caused when the Colorado River, which usually discharges into the Gulf of Mexico, changed course and discharged to the west and north via the Alamo and New Rivers (Rockwell et al., 2022). This change in course would inundate much of the Salton Trough and create a freshwater lake known as Lake Cahuilla, which had a highstand shoreline elevation of ~13 m above sea level. Stratigraphic analyses have revealed evidence for six filling episodes in the past ~1,100 years, with the most recent lake event ending by 1733 CE (Sieh and Williams, 1990; Philibosian et al., 2011; Rockwell et al., 2018; Rockwell et al., 2022). Paleo-shorelines of Lake Cahuilla indicate that this body of freshwater covered much of the sSAF system which indicates that the lake sediments locally record timing of the southernmost sSAF rupture history (Rockwell et al., 2018).

METHODS

Study Sites

We divided ~80 km of the sSAF into five different sections based on where geomorphic features displaying strike-slip evidence are best preserved and most pervasive along the fault (Fig. 17). These sections are in isolated and relatively undisturbed areas where human development is sparse and geomorphic features are well—preserved. To generate slip distribution for the past several surface- rupturing events in each of these sections, we compiled displacement measurements using various piercing points depending on the feature, which included thalwegs of small channels, channel wall margins, and ridge noses. Areas between sections comprise regions where offset features along the fault are buried by young alluvium, are not well-preserved, or have been impacted by recent structural and agricultural developments. Consequently, these sections were deemed unsuitable for our study.

Data Collection

We utilized published geomorphic offset measurements from the southern and northern reaches of the Mecca Hills (Blanton et al., 2020) along with published imagery datasets from UAV and LiDAR surveys (Bunds et al., 2021; Bevis and Hudnut, 2006, respectively). We used the imagery datasets along with Google Earth imagery to determine areas with well-preserved geomorphic features, which were then assessed in the field. Four areas along the fault that are accessible with an off-road vehicle and exhibited well-preserved offset features were selected to collect new, high-resolution imagery. UAV and Real-Time Kinematic (RTK) surveys were conducted at each of these sites and field measurements were obtained by using a standard metric tape measure to quantify geomorphic offset features.

Ground control points (GCPs) were strategically placed on the ground surface along either side of the main fault trace within the survey parameters prior to conducting UAV surveys. These GCPs are placed on benchmarks, or known points on the ground, and can be used to geo-reference imagery with greater accuracy. The total number of GCPs used was determined based on the approximate survey coverage area (Table 2) and ranged from a total of four to nine GCPs. GPS locations of each GCP were collected using an EMLID Reach RS RTK GPS (EMLID, 2022), where base and rover stations were setup in RTK mode with a correction link over Long Range (Lo-Ra) radio. During GPS data collection, the fix status was used to provide decimeter-scale precision between the approximate positioning of the rover to the base station.

Imagery from our new surveys was collected using a DJI Phantom 4 Pro UAV system equipped with a GoPro (Table 2). All flights were conducted using an automated flight mapping application, DroneDeploy, which was operated on a smart phone. Flight parameters were established in DroneDeploy prior to each flight to ensure adequate overlap for Structure-from-Motion-Multiview-Stereo (SfM-MVS) processing techniques and efficient coverage over the areas of interest. Most flight missions were conducted during peak sun hours (11am to 1pm) where shadow coverage is minimal. One flight mission was conducted between 10am and 3pm due to a larger coverage area (Table 2; Fig. 17); however, this did not produce significant shadow effects on the imagery. The altitude above ground level (AGL) for each flight mission was determined from the takeoff point and the UAV system did not adjust to changes in topography during flight missions. As a result, some portions of the flight appeared either closer or farther from the ground level depending on local relief. Changes in local relief for flight missions south of Mecca Hills were relatively insignificant as these locations have gentle or gradually sloping terrain as they are below the shoreline of Lake Cahuilla. The flight mission at Biskra Palms experienced more significant change in local relief as the sSAF in this area is located along the southwestern front of Indio Hills; however, imagery was not negatively impacted. Imagery from published SfM and LiDAR datasets (Bunds et al., 2021; Bevis and Hudnut, 2006, respectively) obtained from the OpenTopography online database were utilized for all other sections of our study area. The SfM dataset from Bunds et al. (2021) covers an area of approximately 40 km^2 from Bombay Beach at the southern terminus of the sSAF to Painted Canyon in the middle of Mecca Hills. DSMs generated from this dataset provide high-resolution imagery with 10 cm/pixel resolution. The LiDAR data from Bevis and Hudnut (2006) covers an extensive area of approximately 1,906 km^2 from Bombay Beach at the southern terminus of the sSAF up to Central California near Coalinga. DSMs generated in this dataset provide imagery with 1 m/pixel resolution, a resolution that allowed examination of larger-scale offsets but smaller-scale features with less than ~5 m of lateral displacement could not be measured with sufficient accuracy.

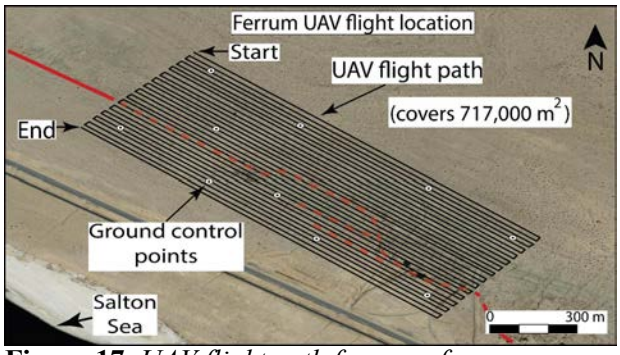

Figure 17. *UAV flight path for one of our surveys located in Ferrum along the northeastern shoreline of the modern-day Salton Sea where the sSAF (red lines) exhibits a double releasing bend. The UAV was flown at an altitude of 30 m above ground level from takeoff point and covered an area of approximately 717,000 m^2. Data derived from this flight produced DSMs and orthomosaics with centimeter-scale accuracy.*

Because the UAV missions were flown at low altitudes (30 m), resolution was obtained at the decimeter-scale.

After imagery collection, offset features were measured in the field with a standard metric tape measure, where the distance between displaced channel margins or channel thalwegs were used as piercing points to project displacement along strike of the fault (Fig. 18). Uncertainty and quality ratings for each offset were estimated similarly to the methodology of Blanton et al. (2020), where the amount of uncertainty was dependent on how well the feature was preserved in the imagery and in the field (i.e., feature quality). Quality ratings were categorized as excellent, good, fair, or poor based on feature quality, preservation, level of erosion, and angle of the feature to the strike of the fault. Features that appeared to be geomorphically offset (ie., channel deflections or meanders) but were not located along the main surficial expression of the fault were determined to be non-tectonic features.

Table 2. *A) (top) UAV Flight Parameters and B) (bottom) UAV Camera Specifications of the 4 new flights performed during this study. Altitude above ground level (AGL) is based on takeoff location. UAV = uncrewed aerial vehicle; GSD = ground sampling distance.*

A	UAV Flight Parameters					
Flight	**Height AGL (m)**	**Date of Flight**	**UAV**	**Total Coverage Area (m^2)**	**Speed (m/s)**	**GSD (cm/pi**
Durmid Hill	30	10/29/2020	DJI P4P	428,000	5	1
Ferrum	30	2/23/2021	DJI P4P	717,000	5	1
Salt Creek	30	11/21 & 12/28/2021	DJI P4P	338,000	5	1
Biskra Palms	30	12/29/2021	DJI P4P	128,000	5	1

B	UAV Camera Specifications				
Flight	**Camera Model**	**Resolution**	**Focal Length**	**Pixel Size**	**Sensor Width**
Durmid Hill	FC6310	4864x3648	8.8mm	2.41µm x 2.41µm	13.2mm
Ferrum	FC6310	4864x3648	8.8mm	2.41µm x 2.41µm	13.2mm
Salt Creek	FC6310	4864x3648	8.8mm	2.41µm x 2.41µm	13.2mm
Biskra Palms	FC6310	4864x3648	8.8mm	2.41µm x 2.41µm	13.2mm

Data Processing

After the new imagery was collected, individual images for each flight mission were examined to ensure quality before processing. Images that were sky-dominated or blurry were manually removed from the datasets and all remaining images were imported into Agisoft Metashape Pro (Agisoft LLC, 2020) to produce geo-referenced models including dense point clouds, Digital Surface Models (DSMs) and orthomosaics. Individual photographs were

orthorectified for topographic distortions and were projected into a real-world coordinate system (World Geodetic System 1984 UTM Zone 11N) to generate the orthomosaics. The processing parameters in Agisoft were set to 'high' for both photo alignment and dense point cloud generation in order to produce high-resolution DSMs and orthomosaics. Setting the processing

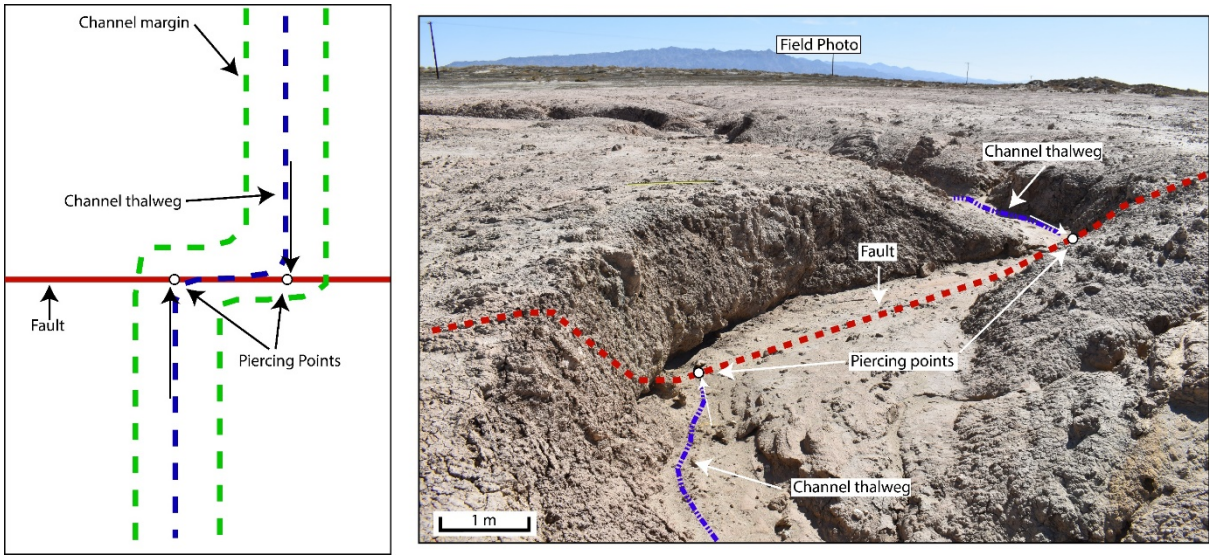

Figure 18. *A) Schematic diagram on measuring the displacement a generalized offset channel by using channel thalwegs as piercing points. Geomorphic features such as channel thalwegs and channel margins are projected into the fault trace to be used as piercing points to resolve displacement. The resulting displacement represents the distance along the fault between the piercing points. Slip vectors on either side of the fault display dextral motion. B) Field photo using the method shown in A. A, modified from Salisbury et al. (2015) and Blanton et al. (2020).*

parameters of the imagery on 'high' allowed for offset features to be observed and measured at the decimeter scale, allowing DSMs to be generated at 1.41 to 1.87 cm/pixel resolution and orthomosaics at 8.2 mm to 1.68 cm/pixel resolution (Table 2). This was deemed to be adequate in terms of product quality and it significantly decreased the amount of time and computational power needed for processing compared to setting the processing parameters on 'highest'. Once DSMs and orthomosaics were generated, they were exported as GeoTIFF files and imported into ArcGIS Pro for additional processing and analysis. Processing in Agisoft was not necessary for published imagery from the UAV and LiDAR datasets because DSMs were already generated and made available for public use on the OpenTopography online database. Instead, the datasets were exported directly from the database and imported into ArcGIS Pro for additional processing and analysis.

As with most methods, processing UAV-based imagery comes with uncertainty. The UAV's internal GPS system has a vertical and horizontal uncertainty of ± 0.5 m and ± 1.5 m, respectively (DJI, 2022) and consequently our georeferenced imagery provides accuracy equal to the UAV system. GCPs used in this study were of equal dimension to those used in Blanton et al. (2020) and measure 26 x 26 cm in area and 29 cm diagonally across. Using these known parameters, they were found to have less than 2.5 cm uncertainty, on average, for relative object accuracy in location. The uncertainty value reflected in the DSMs and orthomosaic imagery we generated are well within the uncertainty ranges of our offset measurements.

Analysis and Interpretation

To enhance visualization of ground surface features, DSMs were imported into ArcGIS Pro to create a variety of maps including hillshade, slope, and contour maps. Hillshade maps were generated using 'multidirectional' settings as opposed to 'traditional' settings, as multidirectional hillshade maps appeared to enhance visualization more efficiently than traditional maps. Contour maps were generated with 10 cm, 50 cm, and 1 m contour intervals, depending on local relief near each offset. Contour maps with 10 cm intervals were generally used for offset features along the northeastern shoreline of the Salton Sea as local relief along the fault in these areas experience minimal variability. Contour maps with 50 cm and 1 m intervals were generally used for offset features located north of the Salton Sea as these areas have more complex local relief along the fault as it leaves the basin and runs through the Mecca and Indio Hills.

All offset features were located using orthomosaic maps exported from Agisoft and hillshade, slope, and contour maps generated in ArcGIS Pro. Field measurements were then verified using the imagery by exporting the maps as JPEG files and importing them into Adobe Photoshop, where each feature was reconstructed to their inferred original configuration by slicing maps along the fault trace, placing each side of the fault into separate layers, and slid, or reconstructed, along the fault until piercing points of the offset feature were realigned. Channel thalwegs were used as piercing points for relatively narrow channels (Fig. 18) and channel wall margins were used as piercing points for relatively wide channels. The files were then imported into Adobe Illustrator, where interpretations were created for original and reconstructed maps. To further verify field and reconstructed measurements, we also used the MATLAB graphical user interface (GUI) LaDiCaoz to assess displacement values for offset features (Zielke and Arrowsmith, 2012). Methods used to measure offset features in LaDiCaoz were the same as the geomorphic methods used in the field and in manual reconstructions of imagery. DSMs were imported into LaDiCaoz to create hillshade maps. Piercing points of each offset along the strike of the fault were defined, and optimal displacement values were generated using goodness-of-fit statistical analyses. Backslipped (reconstructed) models were then autonomously generated based on the optimal displacement values. To further evaluate the accuracy and precision of each method, we plotted each type of measurement against corresponding field measurements to observe any patterns such as strong linear (1:1) correlations, which would suggest a high precision between methods, or where one method was consistently higher or lower than other measurements.

Gaussian distribution analyses were performed in Microsoft Excel with the normal distribution function as a means to evaluate patterns in measured offset data, with data near the mean value having a more frequent occurrence (higher probability) than data further from the mean value. A Gaussian distribution, also called a normal distribution, is a type of continuous probability distribution for a real-valued random variable that represents data symmetrically around the mean (peak) and describes how the values of a variable are distributed. The resulting peaks in the distribution indicate the most probable measurement values of cumulative slip in sequential paleoearthquakes. We chose this method as we know that some measurements have some displacement from pre-event creep whereas other may reflect only co-seismic slip (e.g. Blanton et al, 2020). We expect that the peak values of displacement using a Gaussian distribution method probably reflects the average displacement per event and that the larger values for discrete events may record more efficient transfer of deep seismic offset to brittle offset at the surface which probably include creep from the prior event.

Offset measurements were then divided into separate groups based on similar offset values to assess slip-per-event, with the slip-per-event for each of our sections calculated independently. We interpreted slip in each event by identifying the maximum offset values in each group and calculating the difference in maximum displacement. Using this along with Gaussian distribution analyses can provide insight into the average displacements that occur during large earthquakes along the sSAF and test whether the fault fails with "characteristic" displacement (Schwartz and Coppersmith, 1984) or in a more random nature (Weldon et al., 2005).

RESULTS

A total of 146 geomorphic features were measured along approximately 80 km of the sSAF at Durmid Hill, Salt Creek, Ferrum, Mecca Hills, and Indio Hills (Table 3). Most offsets ranged between 2 and 23 m and were particularly abundant at Salt Creek, Mecca Hills, and Indio Hills, which yielded 12, 52, and 45 offset features, respectively. Geomorphic offset features were not as abundant in other sections due to a combination of the presence of young, active alluvium in some areas that buried the surficial expressions of the sSAF; most of these areas are located below the highstand shoreline of ancient Lake Cahuilla (~13 m above sea level; Philibosian et al., 2011) and as such, have been subjected to multiple filling and desiccation events during repeated lake cycles (Rockwell et al., 2022). Areas where young, active alluvium does not bury the surficial expressions of the sSAF exhibit relatively young geomorphic features that show evidence of preservation through the past 2 to 3 lake cycles.

Most offset features used for this study were located along a single main strand of the fault, with a few being located where the fault is divided into multiple strands. More complicated fault areas typically produce lower overall lateral displacement values. Furthermore, some features were located along what appeared to be inactive strands of the fault or where no fault evidence was detected (Fig. 19). These features were not included in our Gaussian distribution analysis as these features represent areas that no longer produce slip or where the apparent offset was not clearly associated with the fault and was therefore suspect. Offset locations along with orthomosaics, hillshade, slope, and contour maps are shown with examples from each of our five studied sections (Figs. 20 thru 24), to highlight each method of measurement. To assess the accuracy for each measurement method, linear correlations were made between DSM-derived measurements (digital) and field measurements of offset features (Fig. 25). On average, our digital measurements correlated well with field measurements, with some variability. Orthomosaic, hillshade, slope, contour maps, and LaDiCaoz measurements were roughly equal to field measurements, with some features measuring slightly greater or less than the field measurements. Overall, all methods of measurement show relatively strong linear relationships with some variability that fits into the range of measurement uncertainty. Measurements generated from contour maps and LaDiCaoz are considered to be the most accurate methods as contour maps have elevation data derived from DSMs, which produce clearly defined thalwegs and channel walls that aid in eliminating measurement bias, and LaDiCaoz relies on goodness-of-fit statistical analyses to realign geomorphic offset features.

Table 3. *Offset measurements coupled with their respective uncertainties along ~80 km of the sSAF. An uncertainty of 10-30% was assigned to each method depending on factors such as feature quality, erosion, and angle of projected piercing points to the strike of the fault. Quality ratings were assigned as excellent, good, fair, or poor. T = thalweg, SE CW = southeast channel wall, NW CW = northwest channel wall, BH-C = beheaded channel, GE = Google Earth, Ortho = orthomosaic, Williams = Pat Williams' field measurements.*

Offset Master List

Name	Site	Location	Distance along fault (km)	Quality Rating	Feature Type	Google Earth (m)	Ortho (m)	±	Hillshade (m)	±	Slope (m)	±	Contour (m)	±	Williams (m)	Field (m)	±	LaDiCaoz (m)	±	Average (m)	Fault Strand
sSAF-1	Durmid Hill	33.3911677, -115.7604411	5.32	Excellent	T	11.39	N/A	N/A	11.19	1.12	11.20	1.12	11.24	1.12	N/A	10.93	1.09	N/A	N/A	11.19	Main
sSAF-2	Durmid Hill	33.4015008, -115.7790416	7.4	Excellent	T	11.05	N/A	N/A	10.62	1.06	10.70	1.07	10.58	1.06	N/A	10.24	1.02	N/A	N/A	10.64	Main
sSAF-3	Durmid Hill	33.4030709, -115.7814668	7.68	Fair	SE CW	5.58	N/A	N/A	5.42	1.08	5.41	1.08	5.40	1.08	N/A	5.53	1.11	N/A	N/A	5.47	Main
sSAF-4	Durmid Hill	33.4103791, -115.7922758	9	Excellent	T	6.69	N/A	N/A	6.75	0.68	6.78	0.68	6.79	0.68	N/A	6.70	0.67	6.80	0.68	6.75	Minor
sSAF-5	Durmid Hill	33.4104506, -115.7923858	9	Excellent	BH-C	6.69	N/A	N/A	6.75	0.68	6.78	0.68	6.79	0.68	N/A	6.86	0.69	6.80	0.68	6.78	Multiple
sSAF-6	Durmid Hill	33.4104665, -115.7922670	9	Poor	BH-C	3.74	N/A	N/A	3.68	1.10	3.67	1.10	3.63	1.09	N/A	3.28	0.98	N/A	N/A	3.60	Multiple
sSAF-7	Durmid Hill	33.4143044, -115.7978758	9.65	Excellent	T	3.64	N/A	N/A	3.68	0.37	3.65	0.37	3.62	0.36	3.50	3.94	0.39	N/A	N/A	3.67	Main
sSAF-8	Durmid Hill	33.4158879, -115.8002845	9.93	Excellent	T	6.56	6.49	0.65	6.09	0.61	6.12	0.61	6.10	0.61	6.50	6.60	0.66	N/A	N/A	6.35	Main
sSAF-9	Durmid Hill	33.4299834, -115.8193247	12.3	Excellent	NW CW	12.53	N/A	N/A	12.42	1.24	12.45	1.25	12.62	1.26	12.55	11.70	1.17	N/A	N/A	12.38	Main
sSAF-10	Durmid Hill	33.4310865, -115.8209294	12.5	Fair	T	7.39	N/A	N/A	7.19	1.44	7.20	1.44	7.22	1.44	N/A	7.62	1.52	N/A	N/A	7.32	Main
sSAF-11	Durmid Hill	33.4362735, -115.8279458	13.36	Excellent	SE CW	9.13	N/A	N/A	9.25	0.93	9.23	0.92	9.19	0.92	9.00	9.09	0.91	N/A	N/A	9.15	Main
sSAF-12	Salt Creek	33.4383366, -115.8309005	13.72	Good	T	4.19	N/A	N/A	3.89	0.58	4.11	0.62	4.43	0.66	4.00	4.24	0.64	N/A	N/A	4.14	Main
sSAF-13	Salt Creek	33.4436464, -115.8366745	14.52	Excellent	T	3.78	3.58	0.36	3.76	0.38	3.71	0.37	3.68	0.37	3.90	3.66	0.37	3.70	0.37	3.72	Multiple
sSAF-14	Salt Creek	33.4439222, -115.8370470	14.57	Excellent	T	3.80	3.78	0.38	4.00	0.40	4.08	0.41	4.10	0.41	3.50	4.01	0.40	3.90	0.39	3.90	Multiple
sSAF-15	Salt Creek	33.4441250, -115.8373821	14.61	Fair	BH-C	16.65	17.28	3.46	17.72	3.54	17.60	3.52	17.50	3.50	N/A	N/A	N/A	N/A	N/A	17.35	Main
sSAF-16	Salt Creek	33.4445025, -115.8377445	14.66	Excellent	SE CW	12.12	12.48	1.25	12.40	1.24	12.38	1.24	12.52	1.25	12.00	N/A	N/A	12.50	1.25	12.34	Main
sSAF-17	Salt Creek	33.4445025, -115.8377445	14.66	Excellent	BH-C	17.09	16.98	1.70	17.16	1.72	16.76	1.68	17.02	1.70	16.00	N/A	N/A	17.50	1.75	16.93	Main
sSAF-18	Salt Creek	33.4482990, -115.8430715	15.31	Excellent	T	2.48	N/A	N/A	2.58	0.26	2.48	0.25	2.62	0.26	N/A	N/A	N/A	2.40	0.24	2.51	Main
sSAF-19	Salt Creek	33.4482990, -115.8430716	15.36	Excellent	T	2.45	N/A	N/A	2.58	0.26	2.48	0.25	2.62	0.26	N/A	N/A	N/A	2.40	0.24	2.51	Main
sSAF-20	Salt Creek	33.4482990, -115.8430717	15.68	Excellent	T	2.45	N/A	N/A	2.58	0.26	2.48	0.25	2.62	0.26	N/A	N/A	N/A	2.40	0.24	2.51	Main
sSAF-21	Salt Creek	33.4482990, -115.8430718	16.21	Excellent	T	2.45	N/A	N/A	2.58	0.26	2.48	0.25	2.62	0.26	N/A	N/A	N/A	2.40	0.24	2.51	Main
sSAF-22	Salt Creek	33.4482990, -115.8430719	16.33	Excellent	T	2.45	N/A	N/A	2.58	0.26	2.48	0.25	2.62	0.26	N/A	N/A	N/A	2.40	0.24	2.51	Main
sSAF-23	Salt Creek	33.4485574, -115.8434874	16.48	Excellent	BH-C	9.28	9.38	0.94	9.44	0.94	9.44	0.94	9.46	0.95	9.30	10.70	1.07	8.60	0.86	9.45	Main
sSAF-24	Ferrum	33.4505033, -115.8459946	16.49	Excellent	SE CW	4.23	N/A	N/A	4.40	0.44	4.42	0.44	4.38	0.44	4.25	4.34	0.43	4.60	0.46	4.37	Main

sSAF-25	Ferrum	33.4505033, -115.8459946	16.49	Excellent	SE CW	4.20	N/A	N/A	4.40	0.44	4.42	0.44	4.38	0.44	N/A	N/A	N/A	4.60	0.46	4.40	Main
sSAF-26	Ferrum	33.4535323, -115.8504314	17.04	Excellent	SE CW	3.40	N/A	N/A	3.48	0.35	3.39	0.34	3.21	0.32	N/A	3.05	0.31	N/A	N/A	3.31	Main
sSAF-27	Ferrum	33.4542959, -115.8513038	17.06	Fair	SE CW	3.01	N/A	N/A	2.55	0.51	2.53	0.51	2.30	0.46	N/A	2.32	0.46	N/A	N/A	2.54	Main
sSAF-28	Ferrum	33.4555517, -115.8522273	17.37	Good	SE CW	2.80	N/A	N/A	1.33	0.20	1.15	0.17	1.44	0.22	N/A	N/A	N/A	N/A	N/A	1.68	Minor
sSAF-29	Ferrum	33.4556, -115.8520	18.57	Good	SE CW	3.71	N/A	N/A	3.56	0.53	3.58	0.54	3.80	0.57	N/A	N/A	N/A	N/A	N/A	3.66	Minor
sSAF-30	Ferrum	33.4594002, -115.8563058	18.61	Excellent	SE CW	5.77	5.92	0.59	5.88	0.59	5.82	0.58	5.91	0.59	N/A	5.38	0.54	5.10	0.51	5.68	Multiple
sSAF-31	Ferrum	33.4592735, -115.8560647	18.58	Excellent	T	5.78	5.92	0.59	5.88	0.59	5.82	0.58	5.91	0.59	N/A	3.76	0.38	N/A	N/A	5.51	Multiple
sSAF-32	Ferrum	33.4615216, -115.8583188	20.91	Excellent	T	6.84	7.11	0.71	7.00	0.70	6.89	0.69	6.98	0.70	7.00	6.62	0.66	7.10	0.71	6.94	Main
sSAF-33	Ferrum	33.468136, -115.868521	21.87	Good	T	2.52	N/A	N/A	2.50	0.38	2.46	0.37	2.48	0.37	N/A	N/A	N/A	2.60	0.39	2.51	Main
sSAF-34	Ferrum	33.468171, -115.868583	22.25	Good	T	2.65	N/A	N/A	2.50	0.38	2.46	0.37	2.48	0.37	N/A	N/A	N/A	2.70	0.41	2.56	Main
sSAF-35	Ferrum	33.468327, -115.868780	22.31	Good	T	2.10	N/A	N/A	2.50	0.38	2.46	0.37	2.48	0.37	N/A	N/A	N/A	2.60	0.39	2.43	Main
sSAF-36	Ferrum	33.481870, -115.887515	22.67	Good	T	3.16	N/A	N/A	3.62	0.54	3.52	0.53	3.69	0.55	N/A	N/A	N/A	N/A	N/A	3.50	Main
sSAF-37	Ferrum	33.488110, -115.894493	22.94	Good	NW CW	2.81	N/A	N/A	2.74	0.41	2.73	0.41	2.78	0.42	N/A	3.00	0.45	N/A	N/A	2.81	Main
sSAF-38	Ferrum	33.490568, -115.897373	22.96	Fair	T	2.70	N/A	N/A	3.19	0.64	3.14	0.63	3.00	0.60	N/A	N/A	N/A	3.20	0.64	3.05	Main
sSAF-39	Ferrum	33.491198, -115.897309	22.97	Good	T	2.74	N/A	N/A	3.38	0.68	3.20	0.64	3.32	0.66	N/A	2.72	0.54	3.20	0.64	3.09	Minor
sSAF-40	Ferrum	33.493453, -115.900360	23.04	Good	BH-C	3.28	N/A	N/A	3.43	0.51	3.42	0.51	3.40	0.51	N/A	N/A	N/A	N/A	N/A	3.38	Main
sSAF-41	Mecca Hills	33.570947, -115.979608	34	Poor	T	7.75	8.12	1.00	8.16	1.00	7.15	1.00	7.09	1.00	7.60	6.09	1.00	N/A	N/A	7.42	Main
sSAF-42	Mecca Hills	33.571044, -115.979804	34.02	Fair	T	5.04	5.56	0.56	5.46	0.55	5.31	0.53	5.36	0.54	N/A	5.05	0.54	N/A	N/A	5.30	Main
sSAF-43	Mecca Hills	33.571187, -115.979962	34.04	Poor	T	2.62	2.70	0.27	2.46	0.25	N/A	N/A	2.45	0.25	N/A	2.65	0.25	N/A	N/A	2.58	Main
sSAF-44	Mecca Hills	33.571280, -115.979984	34.05	Good	SE CW	3.12	3.16	0.32	3.14	0.31	3.30	0.33	3.24	0.32	4.60	3.20	0.32	N/A	N/A	3.39	Main
sSAF-45	Mecca Hills	33.571280, -115.979984	34.05	Fair	T	8.41	8.49	1.27	8.42	1.26	8.24	1.24	8.58	1.29	8.60	9.75	1.29	N/A	N/A	8.64	Main
sSAF-46	Mecca Hills	33.571528, -115.980288	34.09	Fair	T	N/A	4.96	0.50	4.80	0.48	4.63	0.46	5.00	0.50	N/A	5.10	0.50	N/A	N/A	4.90	Main
sSAF-47	Mecca Hills	33.571578, -115.980337	34.1	Fair	SE CW	N/A	2.58	0.39	2.94	0.44	2.62	0.39	3.04	0.46	N/A	3.10	0.46	N/A	N/A	2.86	Main
sSAF-48	Mecca Hills	33.571578, -115.980337	34.1	Fair	T	N/A	7.33	1.00	7.26	1.00	7.05	1.00	7.10	1.00	N/A	7.10	1.00	N/A	N/A	7.17	Main
sSAF-49	Mecca Hills	33.571644, -115.980419	34.11	Fair	T	N/A	7.44	0.74	7.48	0.75	7.58	0.76	7.57	0.76	N/A	7.20	0.76	N/A	N/A	7.45	Main
sSAF-50	Mecca Hills	33.571644, -115.980419	34.11	Fair	T	N/A	14.62	1.46	14.98	1.50	14.53	1.45	14.85	1.49	N/A	14.70	1.49	N/A	N/A	14.74	Main
sSAF-51	Mecca Hills	33.571691, -115.980476	34.12	Fair	T	N/A	5.15	0.52	5.11	0.51	5.08	0.51	5.30	0.53	N/A	5.40	0.53	N/A	N/A	5.21	Main
sSAF-52	Mecca Hills	33.571910, -115.980710	34.15	Fair	T	N/A	4.70	0.47	4.44	0.44	4.79	0.48	4.98	0.50	N/A	4.60	0.50	N/A	N/A	4.70	Main
sSAF-53	Mecca Hills	33.571910, -115.980710	34.15	Fair	T	N/A	5.12	0.51	4.89	0.49	5.01	0.50	5.19	0.52	N/A	5.20	0.52	N/A	N/A	5.08	Main
sSAF-54	Mecca Hills	33.571910, -115.980710	34.15	Good	T	N/A	12.15	1.22	12.47	1.25	12.20	1.22	12.65	1.27	N/A	12.40	1.27	N/A	N/A	12.37	Main

sSAF-55	Mecca Hills	33.571910, -115.980710	34.15	Good	T	N/A	13.74	1.37	13.60	1.36	13.80	1.38	14.00	1.40	N/A	12.70	1.40	N/A	N/A	13.57	Main
sSAF-56	Mecca Hills	33.572312, -115.981214	34.21	Excellent	SE CW	N/A	3.62	0.54	3.33	0.50	3.51	0.53	3.25	0.49	N/A	4.15	0.49	N/A	N/A	3.57	Main
sSAF-57	Mecca Hills	33.613475, -116.032921	40.88	Excellent	SE CW	4.99	N/A	N/A	4.61	0.46	4.49	0.45	4.69	0.47	5.00	4.65	0.47	N/A	N/A	4.74	Main
sSAF-58	Mecca Hills	33.6138, -116.0333	40.93	Excellent	SE CW	6.93	N/A	N/A	N/A	N/A	N/A	N/A	N/A	N/A	6.75	N/A	N/A	N/A	N/A	6.84	Main
sSAF-59	Mecca Hills	33.613952, -116.033598	40.96	Excellent	SE CW	3.16	N/A	N/A	2.62	0.26	2.60	0.26	2.70	0.27	3.00	3.25	0.33	2.80	0.28	2.88	Main
sSAF-60	Mecca Hills	33.614114, -116.033825	40.99	Excellent	T	N/A	N/A	N/A	N/A	N/A	N/A	N/A	N/A	N/A	2.60	2.51	N/A	N/A	N/A	2.56	Main
sSAF-61	Mecca Hills	33.614247, -116.033987	41.01	Excellent	T	3.15	N/A	N/A	2.62	0.26	2.60	0.26	2.70	0.27	3.00	2.31	0.23	2.20	0.22	2.65	Main
sSAF-62	Mecca Hills	33.614957, -116.034982	41.01	Excellent	T	8.00	N/A	N/A	7.70	0.77	7.75	0.78	7.72	0.77	9.00	8.10	0.81	7.30	0.73	7.94	Main
sSAF-63	Mecca Hills	33.614957, -116.034982	41.01	Good	BH-C	14.20	N/A	N/A	13.50	2.03	13.60	2.04	13.80	2.07	15.00	N/A	N/A	14.30	1.27	14.07	Main
sSAF-64	Mecca Hills	33.616971, -116.037705	41.13	Excellent	T	3.50	N/A	N/A	4.00	0.40	4.18	0.42	4.12	0.41	3.80	4.19	0.42	3.90	0.39	3.96	Main
sSAF-65	Mecca Hills	33.617373, -116.038313	41.47	Excellent	SE CW	21.80	N/A	N/A	22.05	2.21	22.40	2.24	22.50	2.25	22.00	22.60	2.26	22.80	2.28	22.31	Main
sSAF-66	Mecca Hills	33.6182, -116.0395	41.54	Excellent	T	N/A	N/A	N/A	N/A	N/A	N/A	N/A	N/A	N/A	2.70	N/A	N/A	N/A	N/A	2.70	Main
sSAF-67	Mecca Hills	33.6183, -116.0397	41.68	Excellent	SE CW	13.82	N/A	N/A	N/A	N/A	N/A	N/A	N/A	N/A	13.70	N/A	N/A	N/A	N/A	13.76	Main
sSAF-68	Mecca Hills	33.6195, -116.0414	41.71	Good	SE CW	5.10	N/A	N/A	N/A	N/A	N/A	N/A	N/A	N/A	5.30	N/A	N/A	N/A	N/A	5.20	Main
sSAF-69	Mecca Hills	33.6460, -116.0761	41.91	Poor	SE CW	7.01	N/A	N/A	N/A	N/A	N/A	N/A	N/A	N/A	N/A	N/A	N/A	N/A	N/A	7.01	Main
sSAF-70	Mecca Hills	33.647192, -116.077815	46.31	Excellent	T	N/A	N/A	N/A	N/A	N/A	N/A	N/A	N/A	N/A	3.40	N/A	N/A	N/A	N/A	3.40	Main
sSAF-71	Mecca Hills	33.647037, -116.077659	46.5	Fair	T	N/A	5.97	0.60	6.00	0.60	6.01	0.60	5.94	0.59	6.30	6.00	0.59	N/A	N/A	6.04	Main
sSAF-72	Mecca Hills	33.647037, -116.077659	46.5	Fair	T	N/A	13.10	1.31	13.25	1.33	13.26	1.33	13.42	1.34	12.70	13.15	1.34	N/A	N/A	13.15	Main
sSAF-73	Mecca Hills	33.647310, -116.078020	46.52	Excellent	T	10.23	10.35	1.04	10.38	1.04	10.60	1.06	11.00	1.10	N/A	10.00	1.10	N/A	N/A	10.43	Main
sSAF-74	Mecca Hills	33.647833, -116.078657	46.54	Excellent	SE CW	8.24	8.58	0.86	8.80	0.88	8.52	0.85	7.66	0.77	N/A	8.30	0.77	N/A	N/A	8.35	Main
sSAF-75	Mecca Hills	33.648431, -116.079370	46.62	Poor	NW CW	21.50	21.79	3.27	21.00	3.15	20.70	3.11	21.00	3.15	N/A	22.00	3.15	N/A	N/A	21.33	Main
sSAF-76	Mecca Hills	33.649527, -116.080764	46.71	Fair	T	N/A	3.40	0.34	3.30	0.33	3.46	0.35	3.48	0.35	3.50	3.38	0.35	N/A	N/A	3.42	Main
sSAF-77	Mecca Hills	33.6503, -116.0816	46.89	Good	NW CW	N/A	N/A	N/A	12.95	1.94	12.74	1.91	12.66	1.90	11.50	N/A	N/A	N/A	N/A	12.46	Main
sSAF-78	Mecca Hills	33.650555, -116.082039	47.01	Excellent	SE CW	N/A	N/A	N/A	4.22	0.42	4.16	0.42	4.33	0.43	3.50	N/A	N/A	N/A	N/A	4.05	Main
sSAF-79	Mecca Hills	33.650555, -116.082039	47.01	Excellent	SE CW	7.11	6.50	0.65	6.10	0.61	6.90	0.69	6.75	0.68	7.00	5.50	0.68	N/A	N/A	6.55	Main
sSAF-80	Mecca Hills	33.650555, -116.082039	47.01	Good	SE CW	10.32	N/A	N/A	9.86	1.48	9.65	1.45	9.80	1.47	9.20	N/A	N/A	N/A	N/A	9.77	Main
sSAF-81	Mecca Hills	33.650555, -116.082039	47.01	Fair	SE CW	13.62	N/A	N/A	13.48	2.70	13.41	2.68	13.77	2.75	13.00	N/A	N/A	N/A	N/A	13.46	Main
sSAF-82	Mecca Hills	33.650555, -116.082039	47.01	Fair	SE CW	17.59	N/A	N/A	17.02	3.40	16.89	3.38	16.96	3.39	17.50	N/A	N/A	N/A	N/A	17.19	Main
sSAF-83	Mecca Hills	33.650968, -116.082509	47.06	Fair	T	2.80	3.00	0.45	3.10	0.47	3.30	0.50	3.40	0.51	N/A	2.80	0.51	N/A	N/A	3.07	Main
sSAF-84	Mecca Hills	33.650945, -116.082528	47.12	Poor	NW CW	12.50	15.20	2.00	15.13	2.00	15.70	2.00	15.39	2.00	N/A	12.50	2.00	N/A	N/A	14.40	Main

sSAF-85	Mecca Hills	33.650945, -116.082528	47.12	Poor	SE CW	17.10	17.70	2.00	17.60	2.00	17.07	2.00	17.00	2.00	N/A	17.10	2.00	N/A	N/A	17.26	Main
sSAF-86	Mecca Hills	33.6514, -116.0828	47.17	Fair	BH-C	N/A	N/A	N/A	N/A	N/A	N/A	N/A	N/A	N/A	13.00	N/A	N/A	N/A	N/A	13.00	Main
sSAF-87	Mecca Hills	33.651520, -116.083243	47.21	Poor	T	N/A	3.02	0.45	2.95	0.44	3.00	0.45	3.03	0.45	N/A	N/A	N/A	N/A	N/A	3.00	Main
sSAF-88	Mecca Hills	33.651520, -116.083243	47.21	Poor	T	6.07	6.05	0.61	6.36	0.64	6.40	0.64	6.20	0.62	N/A	6.00	0.62	N/A	N/A	6.18	Main
sSAF-89	Mecca Hills	33.651745, -116.083533	47.24	Good	SE CW	5.55	5.40	0.54	5.60	0.56	5.58	0.56	5.50	0.55	N/A	5.52	0.55	N/A	N/A	5.53	Multiple
sSAF-90	Mecca Hills	33.6518, -116.0833	47.25	Excellent	T	14.43	N/A	N/A	14.51	1.45	14.69	1.47	14.60	1.46	N/A	N/A	N/A	N/A	N/A	14.56	Multiple
sSAF-91	Mecca Hills	33.652515, -116.084456	47.36	Good	T	9.45	9.70	0.97	9.65	0.97	9.79	0.98	9.52	0.95	N/A	9.50	0.95	N/A	N/A	9.60	Main
sSAF-92	Mecca Hills	33.652515, -116.084456	47.36	Good	SE CW	N/A	8.10	0.81	8.00	0.80	8.17	0.82	8.08	0.81	N/A	8.50	0.81	N/A	N/A	8.17	Main
sSAF-93	Indio Hills	33.6667, -116.0993	49.47	Good	T	8.42	N/A	N/A	N/A	N/A	N/A	N/A	N/A	N/A	8.50	N/A	N/A	N/A	N/A	8.46	Main
sSAF-94	Indio Hills	33.6727, -116.1061	50.38	Good	T	2.89	N/A	N/A	N/A	N/A	N/A	N/A	N/A	N/A	3.00	N/A	N/A	N/A	N/A	2.95	Main
sSAF-95	Indio Hills	33.673630, -116.107169	50.56	Excellent	SE CW	3.03	N/A	N/A	N/A	N/A	N/A	N/A	N/A	N/A	3.10	N/A	N/A	N/A	N/A	3.07	Main
sSAF-96	Indio Hills	33.673630, -116.107169	50.56	Excellent	SE CW	5.37	N/A	N/A	N/A	N/A	N/A	N/A	N/A	N/A	6.20	N/A	N/A	N/A	N/A	5.79	Main
sSAF-97	Indio Hills	33.673630, -116.107169	50.56	Good	SE CW	9.27	N/A	N/A	N/A	N/A	N/A	N/A	N/A	N/A	10.00	N/A	N/A	N/A	N/A	9.64	Main
sSAF-98	Indio Hills	33.673630, -116.107169	50.56	Good	SE CW	13.61	N/A	N/A	N/A	N/A	N/A	N/A	N/A	N/A	13.20	N/A	N/A	N/A	N/A	13.41	Main
sSAF-99	Indio Hills	33.7450, -116.1921	61.72	Good	T	N/A	N/A	N/A	N/A	N/A	N/A	N/A	N/A	N/A	3.00	N/A	N/A	N/A	N/A	3.00	Main
sSAF-100	Indio Hills	33.7450, -116.1921	61.72	Good	T	N/A	N/A	N/A	N/A	N/A	N/A	N/A	N/A	N/A	3.50	N/A	N/A	N/A	N/A	3.50	Main
sSAF-101	Indio Hills	33.7453, -116.1924	61.76	Good	BH-C	N/A	N/A	N/A	N/A	N/A	N/A	N/A	N/A	N/A	6.00	N/A	N/A	N/A	N/A	6.00	Main
sSAF-102	Indio Hills	33.7463, -116.1936	61.92	Good	T	N/A	N/A	N/A	N/A	N/A	N/A	N/A	N/A	N/A	3.50	N/A	N/A	N/A	N/A	3.50	Main
sSAF-103	Indio Hills	33.7463, -116.1936	61.92	Good	BH-C	N/A	N/A	N/A	N/A	N/A	N/A	N/A	N/A	N/A	10.00	N/A	N/A	N/A	N/A	10.00	Main
sSAF-104	Indio Hills	33.7638, -116.2155	64.72	Good	T	N/A	N/A	N/A	N/A	N/A	N/A	N/A	N/A	N/A	3.30	N/A	N/A	N/A	N/A	3.30	Main
sSAF-105	Indio Hills	33.7638, -116.2155	64.72	Good	BH-C	N/A	N/A	N/A	N/A	N/A	N/A	N/A	N/A	N/A	6.00	N/A	N/A	N/A	N/A	6.00	Main
sSAF-106	Indio Hills	33.768652, -116.222348	65.55	Fair	T	N/A	N/A	N/A	3.62	0.72	3.65	0.73	3.40	0.68	N/A	3.69	0.74	N/A	N/A	3.59	Main
sSAF-107	Indio Hills	33.768738, -116.222449	65.57	Fair	T	3.43	N/A	N/A	3.62	0.72	3.65	0.73	3.40	0.68	3.50	3.60	0.72	N/A	N/A	3.53	Main
sSAF-108	Indio Hills	33.768888, -116.222666	65.58	Fair	T	3.33	N/A	N/A	3.62	0.72	3.65	0.73	3.40	0.68	N/A	N/A	N/A	N/A	N/A	3.50	Main
sSAF-109	Indio Hills	33.769139, -116.222871	65.63	Good	SE CW	1.56	1.54	0.23	1.62	0.24	1.64	0.25	1.60	0.24	N/A	1.76	0.26	N/A	N/A	1.62	Main
sSAF-110	Indio Hills	33.769191, -116.222931	65.64	Good	T	N/A	1.54	0.23	1.62	0.24	1.64	0.25	1.60	0.24	N/A	1.54	0.23	N/A	N/A	1.59	Main
sSAF-111	Indio Hills	33.769364, -116.223095	65.66	Excellent	T	1.57	1.54	0.15	1.62	0.16	1.64	0.16	1.60	0.16	N/A	1.64	0.16	N/A	N/A	1.60	Main
sSAF-112	Indio Hills	33.769584, -116.223331	65.69	Good	T	1.59	1.54	0.23	1.62	0.24	1.64	0.25	1.60	0.24	N/A	1.55	0.23	N/A	N/A	1.59	Main
sSAF-113	Indio Hills	33.7701, -116.2239	65.77	Good	BH-C	N/A	N/A	N/A	N/A	N/A	N/A	N/A	N/A	N/A	8.00	7.88	1.18	N/A	N/A	7.94	Main
sSAF-114	Indio Hills	33.770284, -116.224129	65.8	Good	SE CW	5.00	4.53	0.68	4.49	0.67	4.55	0.68	4.50	0.68	4.50	4.27	0.64	4.30	0.65	4.52	Main

sSAF-115	Indio Hills	33.772643, -116.227389	66.2	Excellent	ridge nose	20.67	20.32	2.03	20.50	2.05	20.40	2.04	20.20	2.02	24.50	23.63	2.36	22.90	2.29	21.64	Main
sSAF-116	Indio Hills	33.772853, -116.227668	66.23	Excellent	T	9.27	9.42	0.94	9.28	0.93	9.50	0.95	9.40	0.94	N/A	8.86	0.89	N/A	N/A	9.29	Main
sSAF-117	Indio Hills	33.772929, -116.227796	66.25	Excellent	T	9.20	9.42	0.94	9.28	0.93	9.50	0.95	9.40	0.94	N/A	8.97	0.90	9.10	0.91	9.27	Main
sSAF-118	Indio Hills	33.813782, -116.273986	71.67	Fair	NW CW	3.38	N/A	N/A	N/A	N/A	N/A	N/A	N/A	N/A	3.10	N/A	N/A	N/A	N/A	3.24	Multiple
sSAF-119	Indio Hills	33.8091, -116.2692	71.85	Good	T	N/A	N/A	N/A	N/A	N/A	N/A	N/A	N/A	N/A	3.80	N/A	N/A	N/A	N/A	3.80	Multiple
sSAF-120	Indio Hills	33.8139, -116.2743	72.55	Excellent	T	N/A	N/A	N/A	N/A	N/A	N/A	N/A	N/A	N/A	3.60	N/A	N/A	N/A	N/A	3.60	Multiple
sSAF-121	Indio Hills	33.8171, -116.2779	73.05	Excellent	T	N/A	N/A	N/A	N/A	N/A	N/A	N/A	N/A	N/A	3.50	N/A	N/A	N/A	N/A	3.50	Multiple
sSAF-122	Indio Hills	33.8270, -116.2940	74.94	Excellent	T	N/A	N/A	N/A	N/A	N/A	N/A	N/A	N/A	N/A	3.70	N/A	N/A	N/A	N/A	3.70	Multiple
sSAF-123	Indio Hills	33.8270, -116.2940	74.94	Excellent	BH-C	N/A	N/A	N/A	N/A	N/A	N/A	N/A	N/A	N/A	8.00	N/A	N/A	N/A	N/A	8.00	Multiple
sSAF-124	Indio Hills	33.8270, -116.2940	74.94	Poor	BH-C	N/A	N/A	N/A	N/A	N/A	N/A	N/A	N/A	N/A	16.50	N/A	N/A	N/A	N/A	16.50	Multiple
sSAF-125	Indio Hills	33.8270, -116.2940	74.94	Poor	BH-C	N/A	N/A	N/A	N/A	N/A	N/A	N/A	N/A	N/A	24.50	N/A	N/A	N/A	N/A	24.50	Multiple
sSAF-126	Indio Hills	33.8299, -116.2980	75.42	Fair	SE CW	12.76	N/A	N/A	12.16	3.65	12.50	3.75	13.01	3.90	N/A	11.46	3.44	N/A	N/A	12.38	Multiple
sSAF-127	Indio Hills	33.8299, -116.2980	75.42	Fair	SE CW	N/A	N/A	N/A	N/A	N/A	N/A	N/A	N/A	N/A	4.10	4.17	1.25	N/A	N/A	4.14	Multiple
sSAF-128	Indio Hills	33.8302, -116.2984	75.47	Good	T	N/A	N/A	N/A	N/A	N/A	N/A	N/A	N/A	N/A	3.30	N/A	N/A	N/A	N/A	3.30	Multiple
sSAF-129	Indio Hills	33.8302, -116.2984	75.47	Good	BH-C	N/A	N/A	N/A	N/A	N/A	N/A	N/A	N/A	N/A	10.00	N/A	N/A	N/A	N/A	10.00	Multiple
sSAF-130	Indio Hills	33.8348, -116.3061	76.35	Fair	BH-C	N/A	N/A	N/A	N/A	N/A	N/A	N/A	N/A	N/A	N/A	3.15	0.95	N/A	N/A	3.15	Main
sSAF-131	Indio Hills	33.8368, -116.3086	76.68	Excellent	SE CW	7.14	N/A	N/A	N/A	N/A	N/A	N/A	N/A	N/A	7.00	N/A	N/A	N/A	N/A	7.07	Main
sSAF-132	Indio Hills	33.8368, -116.3086	76.68	Excellent	SE CW	11.64	N/A	N/A	N/A	N/A	N/A	N/A	N/A	N/A	14.50	N/A	N/A	N/A	N/A	13.07	Main
sSAF-133	Indio Hills	33.8430, -116.3159	77.64	Good	T	3.77	N/A	N/A	N/A	N/A	N/A	N/A	N/A	N/A	4.00	N/A	N/A	N/A	N/A	3.89	Main
sSAF-134	Indio Hills	33.8430, -116.3159	77.64	Good	BH-C	N/A	N/A	N/A	N/A	N/A	N/A	N/A	N/A	N/A	7.60	N/A	N/A	N/A	N/A	7.60	Main
sSAF-135	Indio Hills	33.8430, -116.3159	77.64	Good	BH-C	N/A	N/A	N/A	N/A	N/A	N/A	N/A	N/A	N/A	10.70	N/A	N/A	N/A	N/A	10.70	Main
sSAF-136	Indio Hills	33.8430, -116.3159	77.64	Good	BH-C	N/A	N/A	N/A	N/A	N/A	N/A	N/A	N/A	N/A	14.50	N/A	N/A	N/A	N/A	14.50	Main
sSAF-137	Indio Hills	33.8430, -116.3159	77.64	Good	BH-C	N/A	N/A	N/A	N/A	N/A	N/A	N/A	N/A	N/A	19.00	N/A	N/A	N/A	N/A	19.00	Main
sSAF-138	Indio Hills	33.8430, -116.3159	77.64	Good	BH-C	N/A	N/A	N/A	N/A	N/A	N/A	N/A	N/A	N/A	23.00	N/A	N/A	N/A	N/A	23.00	Main
sSAF-139	Indio Hills	33.8430, -116.3159	77.64	Good	BH-C	N/A	N/A	N/A	N/A	N/A	N/A	N/A	N/A	N/A	26.00	N/A	N/A	N/A	N/A	26.00	Main
sSAF-140	Indio Hills	33.8434, -116.3166	77.72	Excellent	T	N/A	N/A	N/A	N/A	N/A	N/A	N/A	N/A	N/A	3.80	N/A	N/A	N/A	N/A	3.80	Main
sSAF-141	Indio Hills	33.8434, -116.3166	77.72	Excellent	BH-C	N/A	N/A	N/A	N/A	N/A	N/A	N/A	N/A	N/A	7.40	N/A	N/A	N/A	N/A	7.40	Main
sSAF-142	Indio Hills	33.8434, -116.3166	77.72	Excellent	BH-C	N/A	N/A	N/A	N/A	N/A	N/A	N/A	N/A	N/A	10.50	N/A	N/A	N/A	N/A	10.50	Main
sSAF-143	Indio Hills	33.8434, -116.3166	77.72	Excellent	BH-C	N/A	N/A	N/A	N/A	N/A	N/A	N/A	N/A	N/A	14.50	N/A	N/A	N/A	N/A	14.50	Main
sSAF-144	Indio Hills	33.8434, -116.3166	77.72	Excellent	BH-C	N/A	N/A	N/A	N/A	N/A	N/A	N/A	N/A	N/A	19.00	N/A	N/A	N/A	N/A	19.00	Main

sSAF-145	Indio Hills	33.8434, -116.3166	77.72	Excellent	BH-C	N/A	N/A	N/A	N/A	N/A	N/A	N/A	N/A	N/A	25.50	N/A	N/A	N/A	N/A	25.50	Main
sSAF-146	Indio Hills	33.8434, -116.3166	77.72	Excellent	BH-C	N/A	N/A	N/A	N/A	N/A	N/A	N/A	N/A	N/A	28.00	N/A	N/A	N/A	N/A	28.00	Main

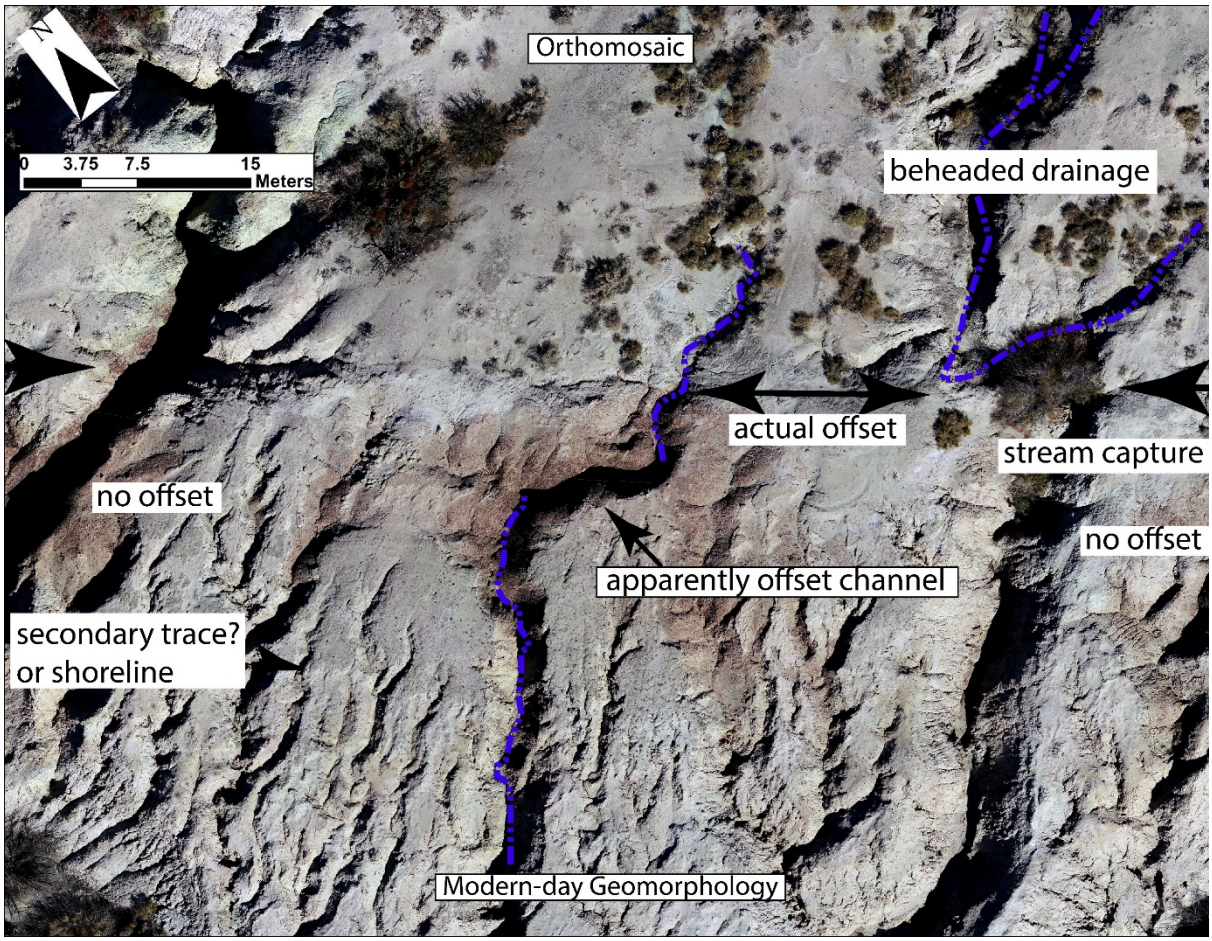

Figure 19. *Fault geomorphology of a site near Salt Creek where the main fault is clearly delineated with a scarp and change in bedrock, with ponded alluvium to the NE. The channel to the right of the figure with a left deflection is interpreted to represent capture by another rill. The channel headwaters are interpreted to be offset from the central channel by about 17 m, which now realigns across the fault. The apparently offset channel does not align with the fault and is interpreted as a meander because channels to the left and right show no deflection at the distance from the main fault. The larger channel on the left of the figure is realigned since the last highstand of lake Cahuilla or has formed since. This apparently deflected channel is not used in our analysis.*

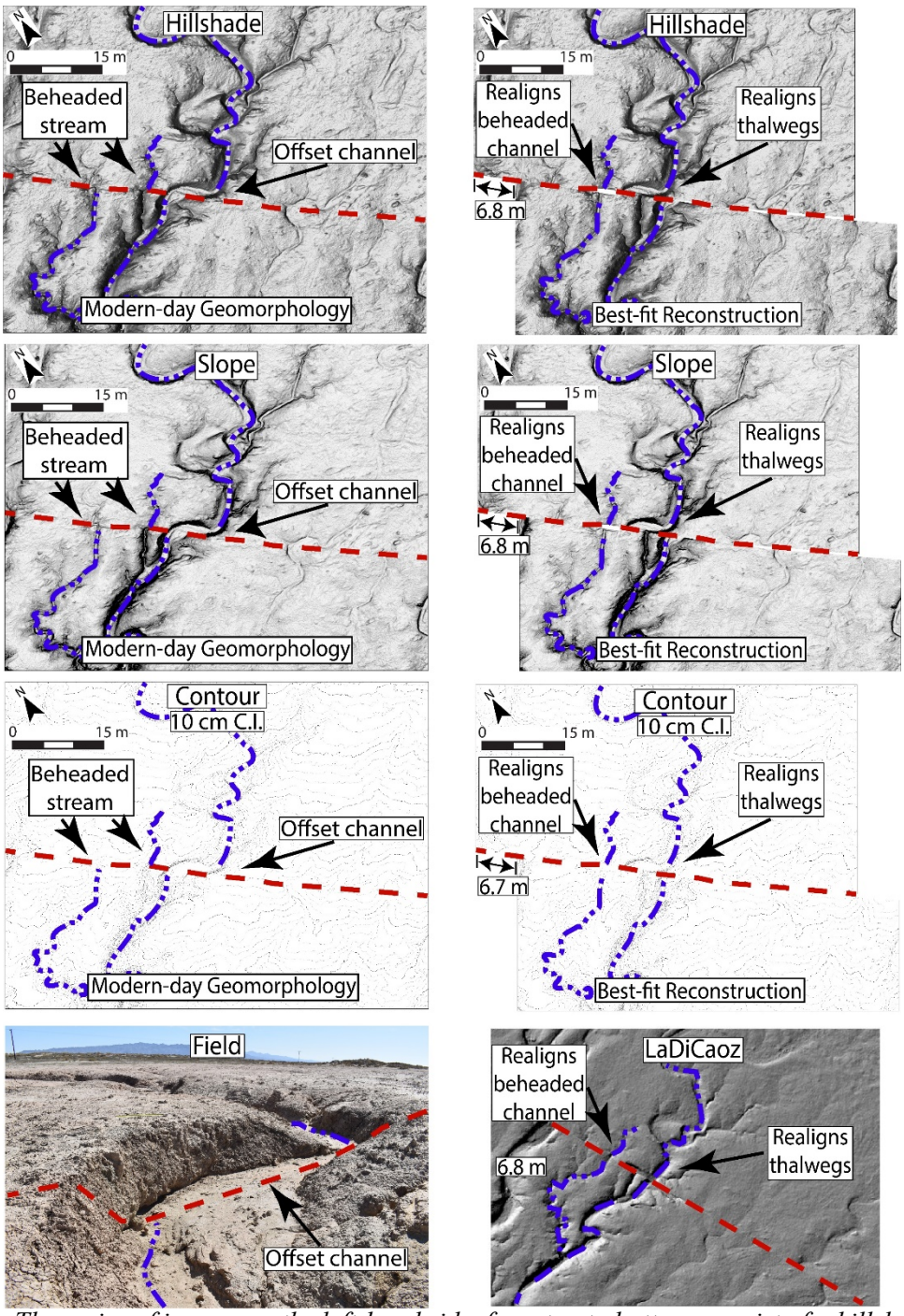

Figure 20. *The series of images on the left-hand side, from top to bottom, consist of a hillshade surface map, slope surface map, contour surface map, and field photograph of offset features sSAF-4 & 5. Dashed red lines represent the surficial fault trace and dashed blue lines represent channel thalwegs. The series of images on the right-hand side, from top to bottom, consist of best-fit reconstructions produced with a hillshade surface map, slope surface map, contour surface map, and a backslipped hillshade surface map model generated in LaDiCaoz.*

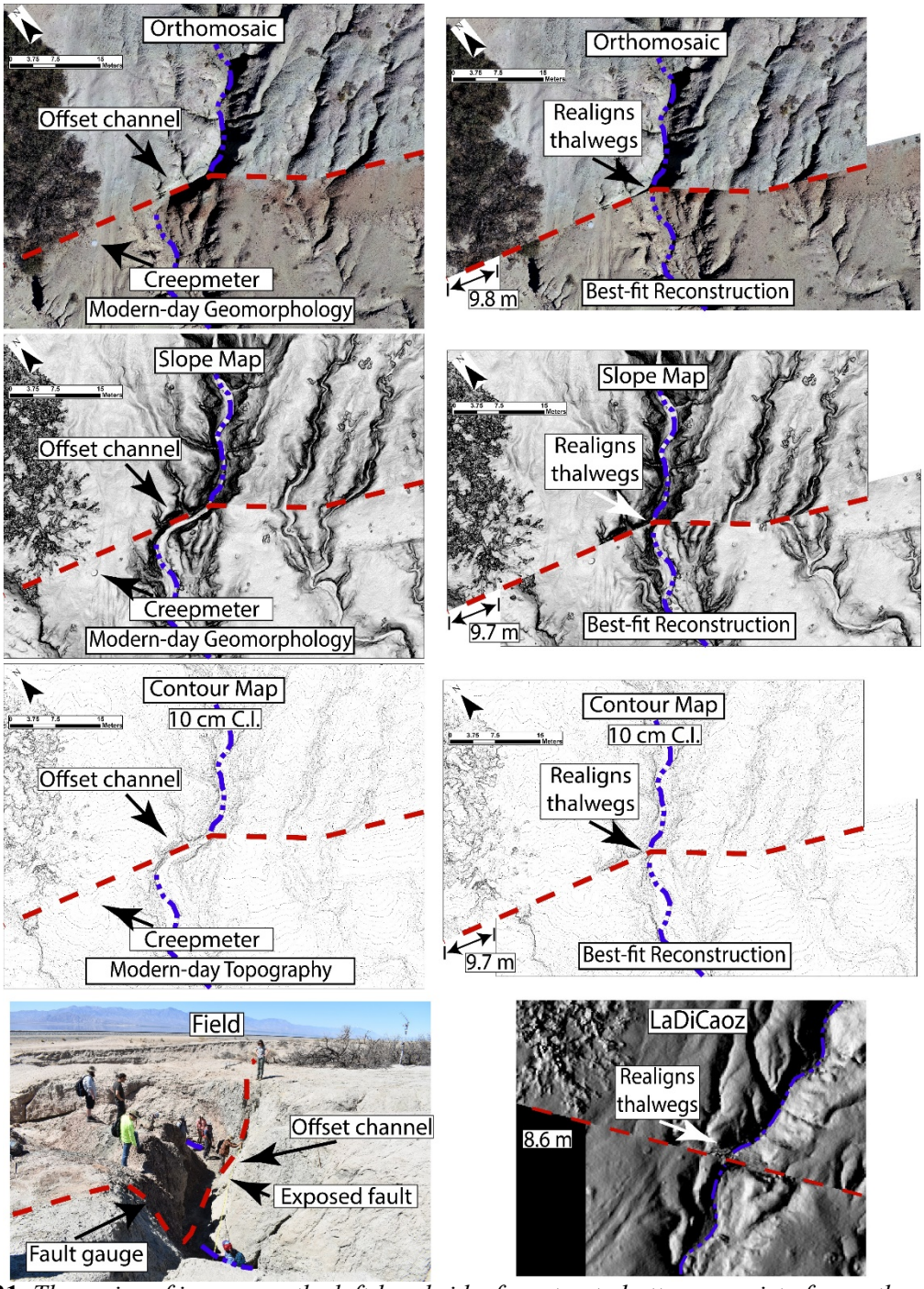

Figure 21. *The series of images on the left-hand side, from top to bottom, consist of an orthomosaic surface map, slope surface map, contour surface map, and field photograph of offset feature sSAF-23. Dashed red lines represent the surficial fault trace and dashed blue lines represent channel thalwegs. The series of images on the right-hand side, from top to bottom, consist of best-fit reconstructions produced with an orthomosaic surface map, slope surface map contour surface map, and a backslipped hillshade surface map model generated in LaDiCaoz.*

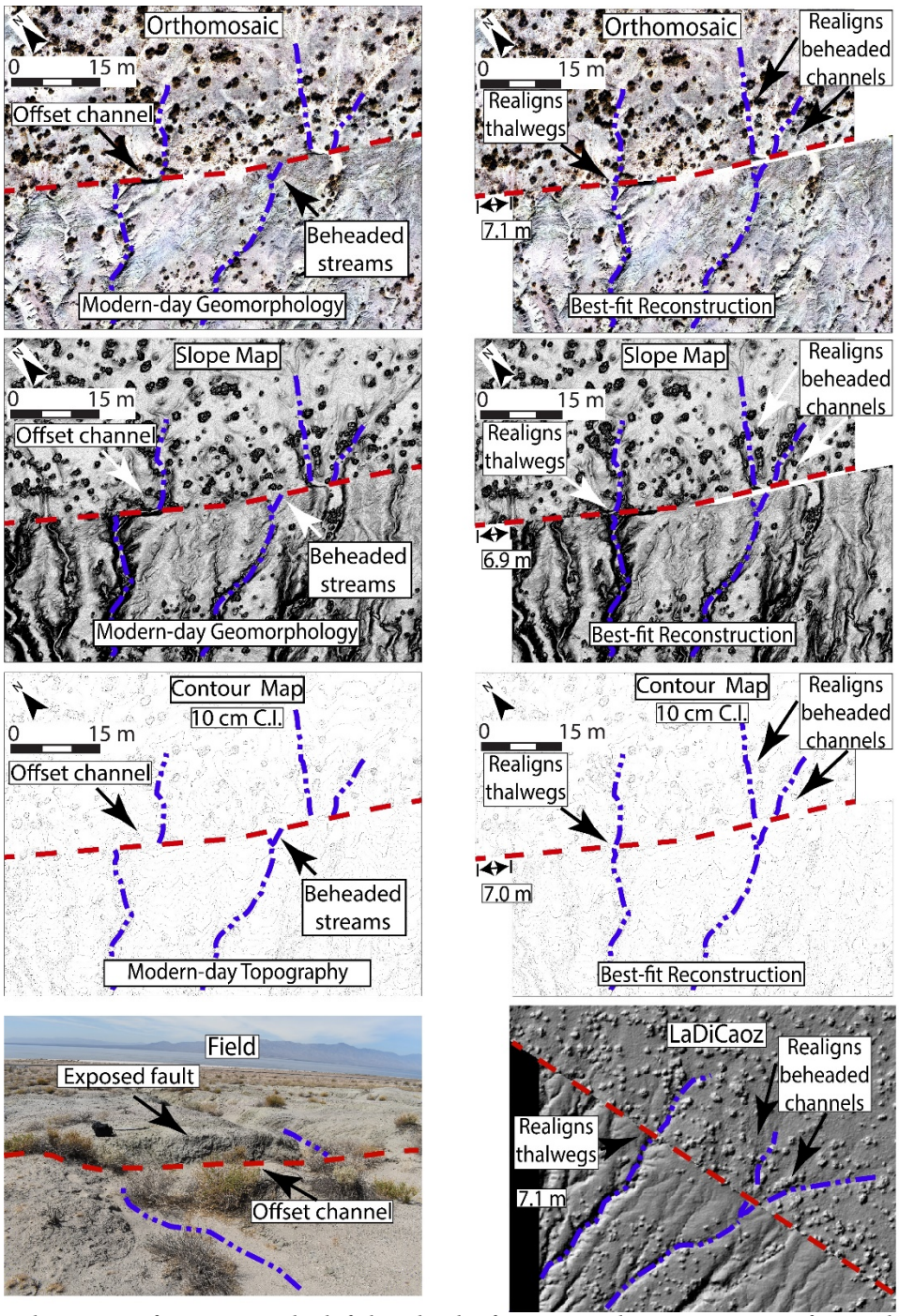

Figure 22. *The series of images on the left-hand side, from top to bottom, consist of an orthomosaic surface map, slope surface map, contour surface map, and field photograph of offset feature sSAF-32. Dashed red lines represent the surficial fault trace and dashed blue lines represent channel thalwegs. The series of images on the right-hand side, from top to bottom, consist of best-fit reconstructions produced with an orthomosaic surface map, slope surface map, contour surface map, and a backslipped hillshade surface map model generated in LaDiCaoz.*

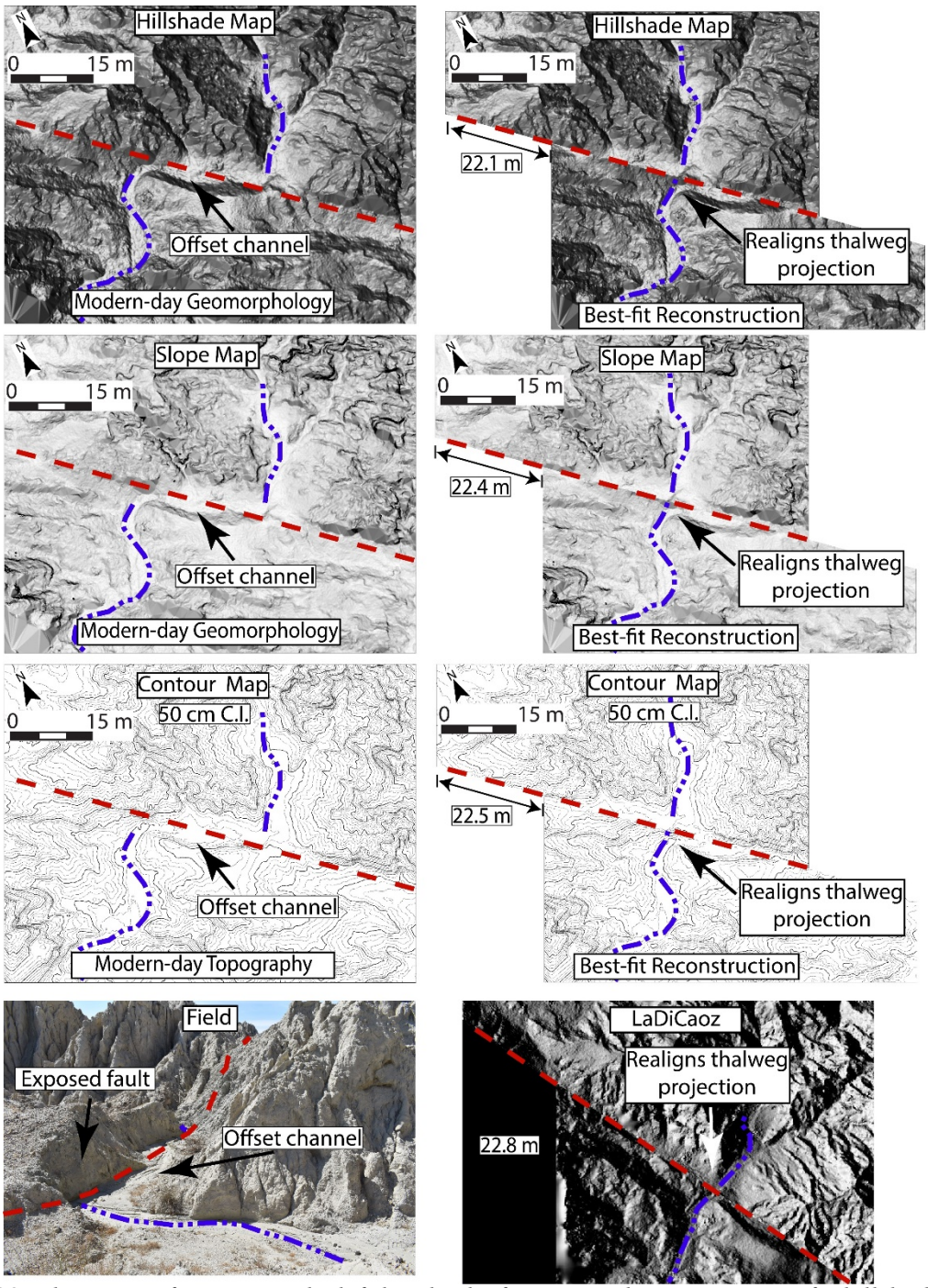

Figure 23. *The series of images on the left-hand side, from top to bottom, consist of a hillshade surface map, slope surface map, contour surface map, and field photograph of offset feature sSAF-75. Dashed red lines represent the surficial fault trace and dashed blue lines represent channel thalwegs. The series of images on the right-hand side, from top to bottom, consist of best-fit reconstructions produced with a hillshade surface map, slope surface map, contour surface map, and a backslipped hillshade surface map model generated in LaDiCaoz.*

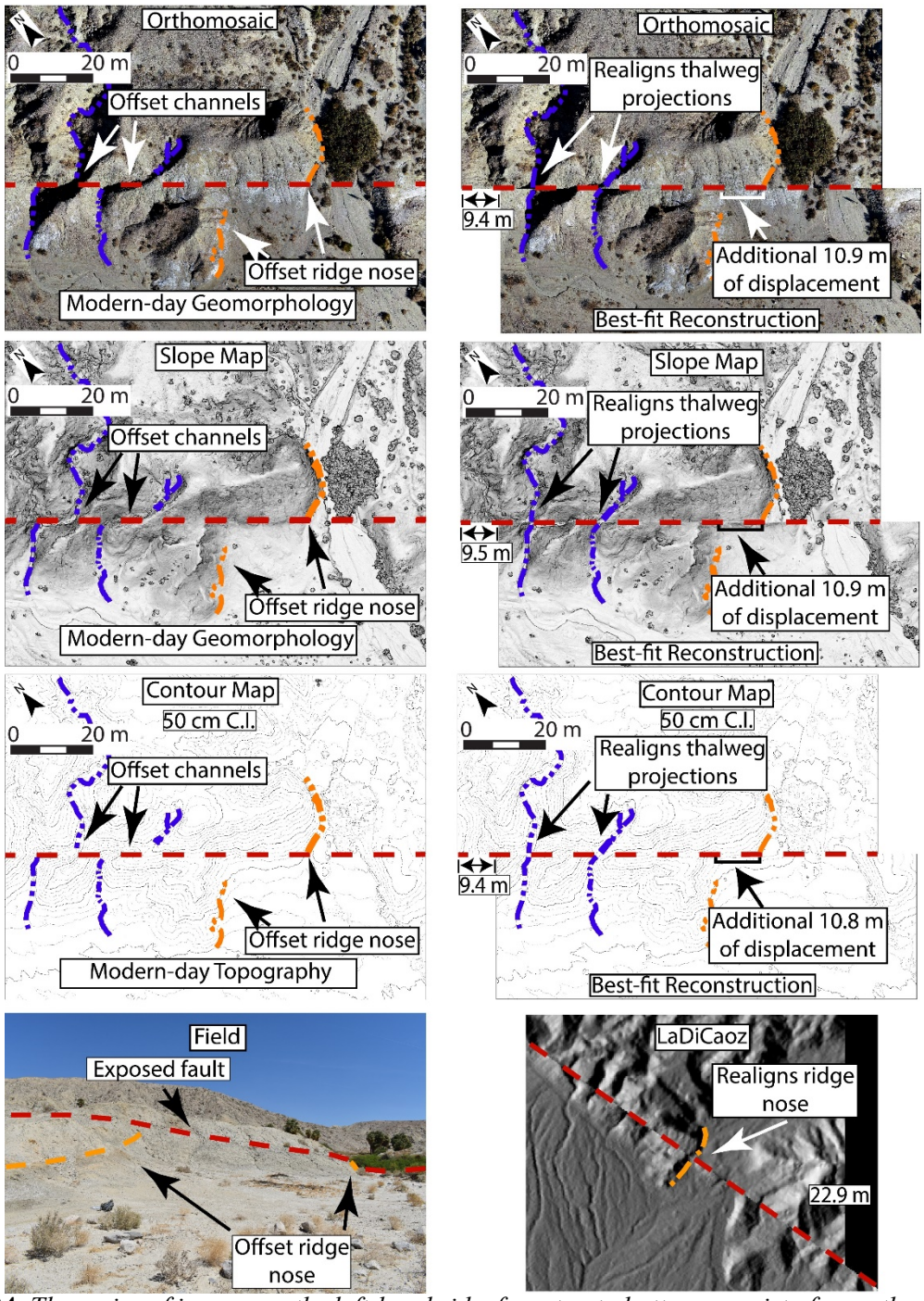

Figure 24. *The series of images on the left-hand side, from top to bottom, consist of an orthomosaic surface map, slope surface map, contour surface map, and field photograph of offset features sSAF-115, 116, & 117. Dashed red lines represent the surficial fault trace, dashed blue lines represent channel thalwegs, and dashed orange lines represent offset ridge nose. The series of images on the right-hand side, from top to bottom, consist of best-fit reconstructions produced with an orthomosaic surface map, slope surface map, contour surface map, and a backslipped hillshade surface map model generated in LaDiCaoz.*

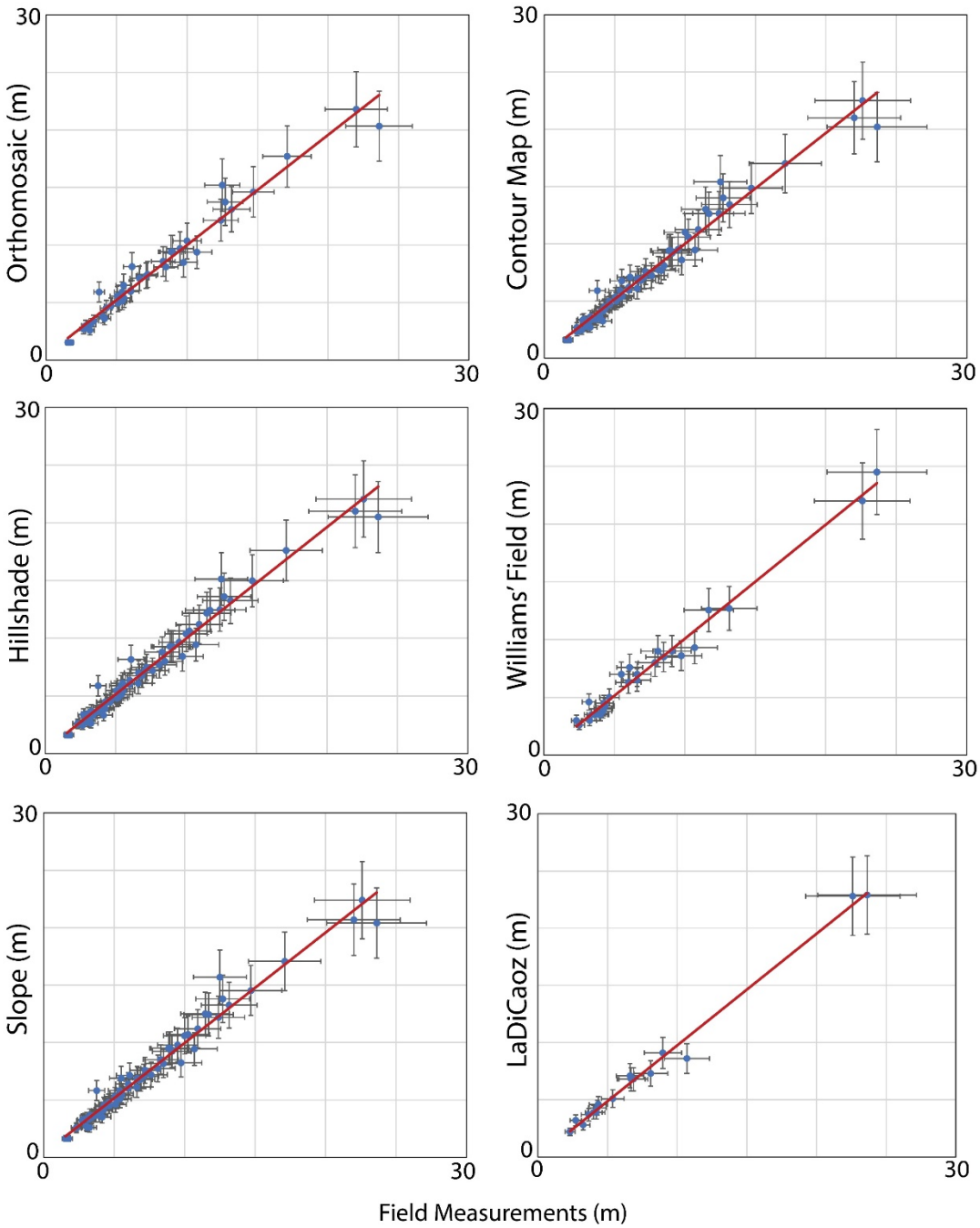

Figure 25. *Linear correlations of the various measurements inferred from digital surface maps (y-axis) compared to field measurements (x-axis) along the sSAF. We also include a linear correlation between field measurements obtained by one of our coauthors 10-15 years ago (Williams; y-axis) compared to new field measurements (x-axis). Only features with both methods of measurements (digital and field) were used in each correlation and all measurements were assigned a 15% uncertainty. The solid red line represents a 1:1 line, which exhibits a strong linear relationship between all measurement methods, with some variability.*

Distribution of offset features along the fault strike show some degree of lateral variability (Fig. 26) with lower overall displacement values where multiple strands are present. Patterns observed in slip distribution along the fault were used to separate clusters of offset features with similar displacement values, and Gaussian distributions were performed to assess the probability of slip-per-event for the past six paleoearthquakes. Analyses from Gaussian distributions reveal six peaks in offset clusters at 3.10, 6.15, 9.4, 13.35, 17.65, 22.1 m, respectively. From these observations, we infer displacement per event to have been 3.1, 3.05, 3.25, 3.93, 4.30, and 4.44 m (Fig. 27) in respective chronological order starting with the MRE. This provides an average value of 3.68 m per event. Distributions for the most recent four events form well-defined peaks, while peaks for older events were poorly defined. Older events correlate to larger-scale offset features, which produce larger uncertainties and are not as abundant as smaller-scale features. Consequently, these features provide relatively sparse data that is broadly distributed, and this results in poorly-defined peaks in the Gaussian distribution analyses.

It should be noted that there were certain sections along the fault where DSM data were analyzed but for which new field measurements were not obtained. In the Indio Hills, field measurements were not obtained within the boundaries of the Coachella Valley Preserve and Pushawalla Palms because of temporary access restrictions. Lastly, offset features in Coachella, located between the Mecca and Indio Hills, have either been entirely removed due to recent anthropogenic development or are located in areas where public access is not readily permitted. Consequently, field measurements were not obtained in these areas. Areas that were not accessible for field measurements in our study were instead assessed using digital imagery and past field measurements obtained by one of our coauthors (Williams) approximately 10-15 years ago.

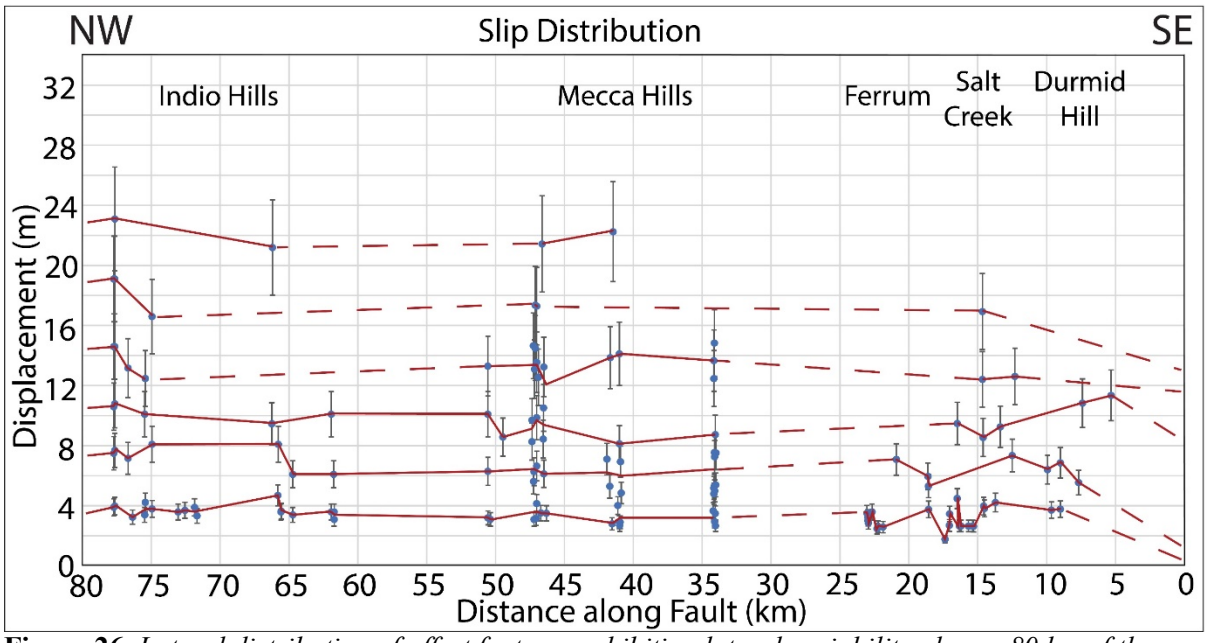

Figure 26. *Lateral distribution of offset features exhibiting lateral variability along ~80 km of the sSAF from Durmid Hill (right) to Indio Hills (left). Displacement of offset features is represented on the y-axis and distance along the fault is represented on the x-axis. Blue dots represent displacement measurements from offset features and trendlines (red) represent average values for slip-per-event. An uncertainty of 15% is assigned for all measurements.*

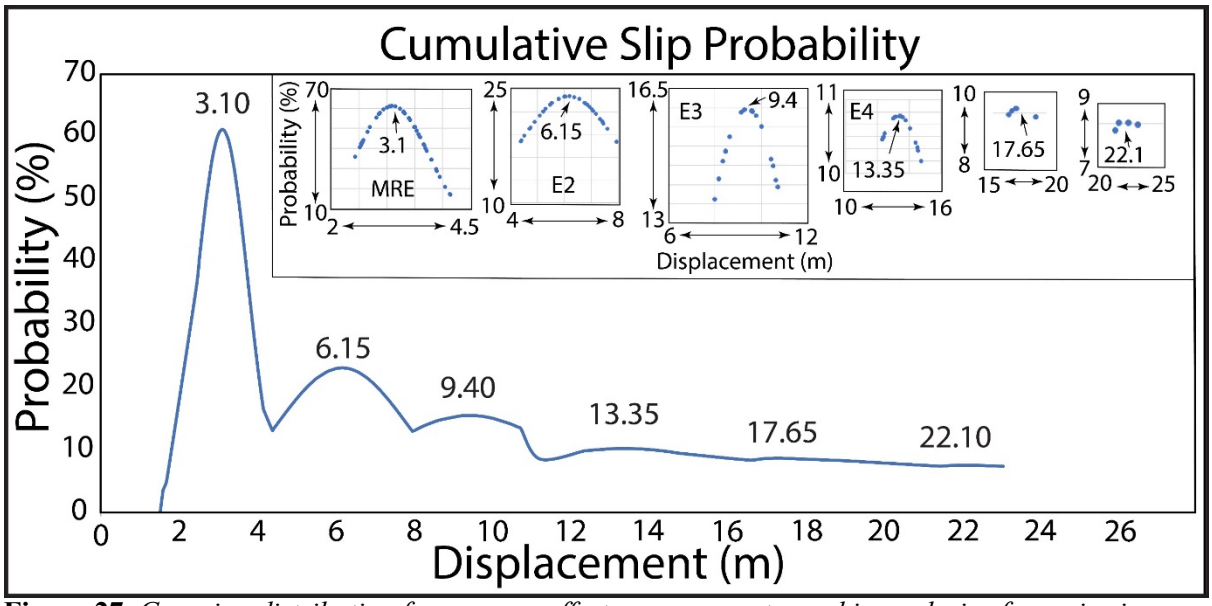

Figure 27. *Gaussian distribution for average offset measurements used in analysis of co-seismic offsets. Six peaks shown in the data represent the highest-probable amount of cumulative displacement for each consecutive event beginning with the MRE (left-most peak). Probability is represented on the y-axis and cumulative displacement is represented on the x-axis. Inset figures exhibit individual data point curves for each respective peak.*

DISCUSSION

Understanding the seismic history along the sSAF is critical to develop accurate seismic hazard assessments to estimate the probability and magnitude of future events. Using offset geomorphic markers to estimate displacement in past earthquakes has proven to be an effective method (Zielke and Arrowsmith, 2012; Salisbury et al., 2012; Dingler et al., 2016; Blanton et al., 2020); however, estimating displacement in past earthquakes has its challenges. The phenomenon of creep and triggered slip can produce slip independently from co-seismic slip events, making them complex variables when resolving displacement from offset geomorphic features. Creep along the sSAF is occurring in its upper 2-3 km at a rate of approximately 3 mm/yr (Lindsey et al., 2014; Sieh and Williams, 1990). Blanton et al. (2020) investigated this phenomenon and showed that the uncertainty in observed offsets are the result of creep that occurs before and after co-seismic offset and should be on the order of 45-60 cm for the sSAF. This level of uncertainty is assumed to be on the same order of magnitude as offset measurement errors, which suggests that slip in an event can be underestimated or overestimated as a result of the 45-60 cm of creep related uncertainty.

Triggered slip was first documented on the southernmost San Andreas fault following the Borrego Mountain earthquake in 1968 (Allen et al., 1972), where 10-25 mm of slip was measured as a result of the shaking. Since then, this phenomenon has been documented along the sSAF resulting from earthquakes such as the 1987 Superstition Hills, 1992 Landers, 1999 Hector Mine, 2010 El Mayor-Cucapah, and 2017 Chiapas earthquakes (Rymer, 2000; Rymer et al., 2002; Wei et al., 2011; Tymofyeyeva et al., 2019). One notable study from Tymofyeyeva et al. (2019) used geodetic and geologic observations to find evidence of triggered slip from the 2017

Mw 8.2 Chiapas earthquake in Mexico, which occurred ~3,000 km away from the sSAF. Evidence of up to 12 mm of triggered slip was found to have occurred along ~40 km of the sSAF from Bombay Beach to Mecca Hills and resulted in a series of cyclic creep events along the sSAF, where slip was observed in mere minutes after nucleation and continued on for more than a year. In the long term, creep is interpreted to integrate intermittent triggered slip between large earthquake events and as such, triggered slip can be integrated with creep (Blanton et al., 2020). Although creep and triggered slip add complexity when resolving displacement, offset features displaying less than ~1 m of lateral displacement were not considered in our study as these features likely reflect modern creep and triggered slip events, which post-date the most recent surface rupturing event around ca 1726 AD (Rockwell et al., 2018). Meter-scale offset features such as those observed in this study are interpreted to be the result of a combination of creep and triggered slip coupled with co-seismic slip from past earthquakes (Blanton et al., 2020). Eliminating the inclusion of decimeter-scale offset features helped to resolve past displacement events along the sSAF with minimal uncertainty. We believe that it is a useful and reasonable assumption to group interseismic creep with the prior segment rupture. This assumption simplifies interpretation of the geomorphic offset record and we believe it is unlikely that any of the preserved offsets exaggerate prehistoric coseismic displacement.

Our results show that slip distribution varies along strike of the fault, and average slip-per-event estimates range between 3.1 to 4.4 m of lateral displacement per event for the past six large surface rupturing earthquakes – yielding an average of 3.68 m of displacement per event. Average slip-per- event estimates for the past four earthquakes, in which data is most abundant, range between 3.1 to 3.93 m of lateral displacement per event – yielding an average of ~3.33 m of displacement per event. These estimates agree well with other studies along the sSAF (Blanton et al., 2020; Dingler et al., 2016). Using the ~3.33 m of average displacement from the past four events and applying the 180-year average recurrence interval (Philibosian et al., 2011) yields a slip rate along the sSAF of about 18.5 mm/yr, which agrees well with previous studies (Behr et al., 2010; Lindsey et al., 2014). Another way to assess the rate is to use the ages of past events from paleoseismology and assume that the four events recognized from offset geomorphic features corresponds to the past four paleoseismic events determined by Philibosian et al. (2011) but corrected for the age of the lake by Rockwell et al. (2022). The events Coa3 and Coa4 were reinterpreted as a single event by Rockwell et al. (2022) as they occurred during the rising stages of Lake C. Coa4 occurred during Lake D, which is dated to 1192-1241 CE. Using the displacement of the past four events at 13.3+1.4/-2.1 m and the time since the first event as 1225+/-25 CE, or about 800 years, yields a slip rate of 16.6 mm/yr but with a longer than average open window which should slightly reduce the inferred rate. Both rate estimates fall within the 16-18 mm/yr range of published rates.

The displacement estimates revealed in the Gaussian distribution analysis align well for the past four large, surface rupturing events resulting in peak displacements of 3.10, 3.05, 3.25, and 3.93 m, respectively. Peaks for older events are not well resolved, likely because the data for these events is too sparse to discern peak displacements or because the displacement amounts for these older events are different from the four most recent events. Older events displaying larger displacement are subjected to the greatest amount of uncertainty compared to smaller, more recent offsets. This is in part due to the lack of abundance for large-scale offsets as these features have been subjected to more erosion and stream capture, particularly for features located below the highstand shoreline of ancient Lake Cahuilla, which may have removed evidence produced by older events.

On average, past large earthquake events along the sSAF to the south of the Indio Hills occurred every ~180 years (Philibosian et al., 2011) and occurred between every 380-640 years to the north of the Indio Hills (Castillo et al., 2021). This implies that not all large ruptures occurring south of or within the Indio Hills continue to rupture north along the Banning fault. This would also account for the lower slip rate determined for the Banning fault north of highway 62 (Gold et al., 2015), which also suggests a lower amount of slip per event, as suggested by Castillo et al. (2021).

The latest significant rupture of the sSAF occurred around 1726 CE (Rockwell et al., 2018) which indicates an open interval of about 300 years. This long open interval between earthquakes has led to speculation that the sSAF is due for a relatively large surface rupturing event. Brothers et al. (2011) notes that although it is commonly believed that the fault is ~100 years overdue for a large earthquake event, this might not be the case due to the absence of rapid stress loading induced by cyclic flooding events from Lake Cahuilla which may be contributing to the prolonged seismic quiescence. Whether this holds to be true or not, substantial dextral elastic loading has accumulated during the present unusually long open interval. Observed strain rates from geodetic evidence along the sSAF suggest that the fault has accumulated a slip deficit during this recent seismic quiescence of up to 5.5-7.0 m, if slip rates are relatively constant over the past several sSAF seismic cycles (Fialko, 2006), which is comparable to past co-seismic offsets recorded along the fault to the north (Zielke et al., 2010). This leads to further speculation on how the accumulated slip deficit will be distributed – will the fault release all accumulated slip in one large earthquake or two smaller events with displacement similar to the past four ruptures (i.e. “characteristic slip”)? If the potential slip accumulated across the fault during the current 300-yearquiescent period is related to the absence of lake loading, it is plausible that the fault is stronger in dry conditions (Brothers et al., 2011; Hill et al., 2020) and could release the entire amount of inferred accumulated slip in a single event. Hill et al. (2020) explain that as pore pressures decrease, the underlying bedrock becomes stronger; however, the degree to which it gets stronger is relevant to tectonically driven slip rates. If this holds true and slip rates along the sSAF have remained constant in the recent geologic past, the next large event could produce lateral displacement on the order of 4.8-5.4 m based on 300 years of accumulation at 16-18 mm/yr. We note that if rupture displacement magnitude plays a role in how often the sSAF propagates through San Gorgonio Pass, and if 5 m or greater displacement occurs in the next earthquake, it is reasonable to assume that the next event may extend beyond the confines of the Salton Trough (or vice versa).

Observationally based time- and slip-predictable models of earthquake occurrence have been invoked to estimate the size of future earthquakes based on the lapse time since the most recent event, or the timing of future earthquakes based on the amount of slip in the most recent event along with the loading rate (Shimazaki and Nakata, 1980). The time-predictable model states that an earthquake will only occur when the stress relieved in the prior earthquake has been re-accumulated whereas the slip- predictable model states that all the stress accumulated since the prior earthquake is released in the next event (Rubinstein et al., 2012) which implies that greater time intervals between two events produce earthquakes of greater size. In these models the basic assumption is that the general characteristics that regulate fault strength have not changed significantly. However, in the case of the sSAF, this is likely not the case because of the fluctuating lake levels (Luttrell et al., 2007; Hill et al., 2020). Similarly, the characteristic earthquake model (Schwartz and Coppersmith, 1984) may not apply because of the changes in fundamental fault properties. Hence, the speculation that the southernmost San Andreas fault is

"overdue" may be a misnomer and should probably left as an unknown until time-dependent offset or slip rate date may be developed to evaluate whether a dry lake may delay rupture.

An earthquake causing 5-6 m of displacement along the sSAF could have devastating effects on the population of southern California as the fault also crosses all of the major highway systems coming in and out of southern California leading to the east, all of the water supply lines going into Los Angeles from the Colorado River, most of the water supply lines going into San Diego, and a majority of the water canals used for irrigation in the Salton Trough. More notably, if a large earthquake occurs along the sSAF and produces a rupture that propagates through San Gorgonio Pass, it has the potential to cause significant damage in Los Angeles and the surrounding areas due to focusing and basin effects (Olsen et al., 2006). Earthquake scenario models where nucleation occurs along the southern terminus of the sSAF and travels northward show that if the rupture propagates past San Gorgonio Pass, it can travel through the San Bernardino, Chino, San Gabriel, and Los Angeles basins (Olsen et al., 2006), regions that can trap seismic energy and channel it into the Los Angeles region. If all ~5 m of slip is released along the sSAF in the next event, the rupture may propagate northward into the densely populated Los Angeles region, producing what is believed to be the "worst-case scenario" for a large San Andreas earthquake.

CONCLUSION

We obtained imagery datasets from previously published LiDAR and SfM surveys, along with very-high-resolution SfM imagery we obtained from new UAV surveys during this study, to identify and measure a total of 146 tectonically offset geomorphic features along the southernmost ~80 km of the San Andreas fault between Bombay Beach and Indio Hills. From these observations, we derive the slip distribution and slip-per-event for the past several large, surface rupturing earthquakes. Most offsets observed in this study exhibit displacements ranging from 2 to 23 m and provide evidence for displacement for the past six earthquake events. Slip measurements derived from this study were used in a Gaussian analyses, which reveal six peak cumulative displacements of 3.1, 6.15, 9.4, 13.35, 17.65, 22.1 m, respectively, in which we infer average slip-per-event for the past six earthquakes to have been 3.1, 3.05, 3.25, 3.93, 4.30, and 4.44 m in respective chronological order starting with the MRE. The most recent four events with smaller, well-preserved offsets provide distributions which form well-defined peaks; however, older events with large-scale offsets are not as well resolved, which is partly due to the lack of data for these larger features as they have been exposed to more stream capture and erosion through time which may have removed evidence produced by older events, particularly for offset features located below the highstand shoreline of ancient Lake Cahuilla. Consequently, we determined a range for slip rate by first using the average displacement from the past four events (~3.33 m) along with the 180-year average recurrence interval to derive a slip rate of approximately 18.5 mm/yr. Next, we used the cumulative displacement of the past four events (~13.3 m) and the time since the occurrence of the 4th paleoseismic event (~800 years) to derive a slip rate of approximately 16.6 mm/yr. This provides an estimated range for slip rate between 16.6-18.5 mm/yr along the sSAF, which is comparable to other published geologic slip rates in the region. Given this slip rate, coupled with published paleoseismic earthquake ages, an average recurrence interval of 180 years, and our current 300-year open interval between large events, the sSAF may have accumulated a slip deficit on the order of 4.8-5.4 m. This leads to speculation on if the accumulated slip will be released in one or two events, the latter of which assumes displacement comparable to the previous four events. Some studies suggest that the sSAF is

"overdue" given the current seismic quiescence; however, it is possible that the lack of lake loading from ancient Lake Cahuilla is playing a role in the delayed interval since the MRE. It is conceivable that the fault is stronger in dry conditions and if true, an earthquake nucleating along the sSAF could release all accumulated slip in the next large event. If this is the case, it is possible that the sSAF will produce large enough displacement to cause a rupture to propagate northward out of the limits of the Salton Trough, through San Gorgonio Pass, and possibly beyond, which could channel seismic energy into the Los Angeles basin and surrounding regions. Such an event could produce what some have speculated to be the "big one" (greatest damage cost) for an earthquake along the San Andreas fault.

DECLARATION OF COMPETING INTERESTS

The authors declare no competing interests.

DATA AND RESOURCES

Imagery from existing LiDAR and Structure-from-Motion surveys used in this research came from published sources listed in the references. New imagery collected during this research has been uploaded to OpenTopography for free public access.

The electronic supplement to this paper presents the offsets and reconstructions of all new interpreted offsets along the southernmost ~80 km of the San Andreas fault from Bombay Beach northwest into the Indio Hills along with new aerial imagery collected during this study.

ACKNOWLEDGEMENTS

This research was supported and funded by the USGS Earthquake Hazards Program (Award No. G21AP10005, Rockwell and Gontz). We appreciate the field support of Lauren Booth, Faith Burkett, and Zoe Morgan for their assistance with UAS and RTK GPS surveys for this research. We thank Red Jeep Tours by Desert Adventures for access along their private roads near Biskra Palms, and Eagle Mountain Mining and Railroad for access at Ferrum. Finally, we thank Anonymous for their comprehensive reviews which greatly enhanced this paper.

References Cited

Agisoft LLC (2020). Agisoft Metashape User Manual: Professional Edition, Version 1.6, 1-172, accessed 20th Jan 2022.

Allen, C.R., Wyss, M., Brune, J.N., Granz, A., and Wallace, R.E. (1972). Displacements on the Imperial, Superstition Hills, and San Andreas faults triggered by the Borrego Mountain earthquake, in the Borrego Mountain earthquake of April 9, 1968: U.S. Geol. Surv. Prof. Pap. 787, 87-104.

Behr, W.M., Rood, D.H., Fletcher, K.E., Guzman, N., Finkel, R., Hanks, T.C., Hudnut, K.W., Kendrick, K.J., Platt, J.P., Sharp, W.D., Weldon, R.J., and Yule, J.D. (2010). Uncertainties in slip-rate estimates for the Mission Creek strand of the southern San Andreas fault at Biskra Palms Oasis, southern California, Bulletin of the Geological Society of America, **122**, Issue 9-10, 1360-1377, doi: 10.1130/B30020.1.

Bevis, M. and Hudnut, K. (2006). B4 Lidar Project: Airborne Laser Swath Mapping (ALSM) survey of the San Andreas Fault (SAF) system of central and southern California, including the Banning segment of the SAF and the San Jacinto fault system. National Center for Airborne Laser Mapping (NCALM), U.S. Geological Survey, the Ohio State University, and the Southern California Integrated GPS Project. Distributed by OpenTopography, doi: https://doi.org/10.5066/F7TQ5ZQ6.

Blanton, C.M., Rockwell, T.K., Gontz, A.M., and Kelly, J.T. (2020). Refining the spatial and temporal signatures of creep and co-seismic slip along the southern San Andreas Fault using very high resolution UAS imagery and SfM-derived topography, Coachella Valley, California: Elsevier, Geomorphology, **357**, 107064, doi: https://doi.org/10.1016/j.geomorph.2020.107064.

Brothers, D., Driscoll, N.W., Kent, G.M., Harding, A.J., Babcock, J.M., and Baskin, R.L. (2009). Tectonic evolution of the Salton Sea inferred from seismic reflection data: Nature Geoscience, **2**, 581–584, https://doi.org/10.1038/ngeo590.

Brothers, D., Kilb, D., Luttrell, K., Driscoll, N., and Kent, G. (2011). Loading of the San Andreas fault by flood-induced rupture of faults beneath the Salton Sea: Nature Geoscience, **4**, 486–492, https://doi.org/10.1038/ngeo1184.

Bunds, M., Scott, C., Whitney, B., and Lee, V.J.C. (2021). New SfM data over the Southern San Andreas Fault, CA, distributed by OpenTopography, doi: https://opentopography.org/news/new-sfm-data-over-southern-san-andreas-fault-ca.

Castillo, B.A., McGill, S.F., Scharer, K.M., Yule, D., McPhillips, D., McNeil, J., Saha, S., Brown, N.D., and Moon, S. (2021). Prehistoric earthquakes on the Banning strand of the San Andreas fault, North Palm Springs, California, Geosphere, **17**, no. 3, 685-710, https://doi.org/10.1130/GES02237.1.

Dingler, J., Driscoll, N., Seitz, G., and Kent, G. (2016). New quantitative constraints on Holocene slip rate and surface displacement along the southern San Andreas fault in the Mecca Hills using ground based terrestrial laser scanning: in Anderson R. Anderson, and H. Ferriz (Eds.), Applied Geology in California: Association of Environmental and Engineering Geologists Special Publication, **26** (2016), 809-832.

DJI (2022). Phantom 4 Pro Specs, https://www.dji.com/phantom-4-pro/info#specs, accessed 10th Jan 2022.

EMLID (2022). Reach RS+ (EMLID), https://emlid.com/reachrs/, accessed 10th Jan 2022.

Fialko, Y. (2006). Interseismic strain accumulation and the earthquake potential on the southern San Andreas fault system, Nature, **441**, 968-971, doi: 10.1038/nature04797.

Field, E.H., and 2014 Working Group on California Earthquake Probabilities (2015). UCERF3: A New Earthquake Forecast for California's Complex Fault System: U.S. Geological Survey Fact Sheet 2015–3009, 1-6, http://dx.doi.org/10.3133/fs20153009.

Field, E.H., Arrowsmith, J.R., Biasi, G.P., Bird, P., Dawson, T.E., Felzer, K.R., Jackson, D.D., Johnson, K.M., Jordan, T.H., Madden, C., Michael, A.J., Milner, K.R., Page, M.T., Parsons, T., Powers, P.M., Shaw, B.E., Thatcher, W.R., Weldon, R.J., and Zeng, Y. (2014). Uniform California Earthquake Rupture Forecast, Version 3 (UCERF3)—The time-independent model: Bulletin of the Seismological Society of America, **104**, 1122–1180, https://doi .org/10.1785/0120130164.

Fuis, G.S. and Mooney, W.D. (1990). Lithospheric structure and tectonics from seismic-refraction and other data, The San Andreas Fault System, California (textbook): U.S. Geological Survey Professional Paper 1515, 207-236.

Fumal, T.E. (2002). Timing of Large Earthquakes since A.D. 800 on the Mission Creek Strand of the San Andreas Fault Zone at Thousand Palms Oasis, near Palm Springs, California: Bulletin of the Seismological Society of America, **92**, 2841-2860, doi: 10.1785/0120000609.

Gold, P.O., Behr, W.M., Rood, D., Sharp, W.D., Rockwell, T.K., Kendrick, K., and Salin, A. (2015). Holocene geologic slip rate for the Banning strand of the southern San Andreas

Fault, southern California, Journal of Geophysical Research: Solid Earth, **120**, Issue 8, 5639-5663, doi:10.1002/2015JB012004.

Lindsey, E.O., Fialko, Y., Bock, Y., Sandwell, D.T., and Bilham, R. (2014). Localized and distributed creep along the southern San Andreas Fault, Journal of Geophysical Research: Solid Earth, 7909-7922, doi: 10.1002/2014JB011275.

Luttrell, K., Sandwell, D., Smith-Konter, B., Bills, B., and Bock, Y. (2007). Modulation of the earthquake cycle at the southern San Andreas fault by lake loading, Journal of Geophysical Research, **112**, B08411, 1-15, doi:10.1029/2006JB004752.

Olsen, K.B., Day, S.M., Minster, J.B., Cui, Y., Chourasia, A., Faerman, M., Moore, R., Maechling, P., and Jordan, T. (2006). Strong shaking in Los Angeles expected from southern San Andreas earthquake: Geophysical Research Letters, **33**, L07305, https://doi.org /10.1029/2005GL025472.

Philibosian, B., Fumal, T., and Weldon, R. (2011). San Andreas Fault Earthquake Chronology and Lake Cahuilla History at Coachella, California: Bulletin of the Seismological Society of America, **101**, 13–38, doi:10.1785/0120100050.

Rockwell, T.K., Meltzner, A.J., and Haaker, E.C. (2018). Dates of the Two Most Recent Surface Ruptures on the Southernmost San Andreas Fault Recalculated by Precise Dating of Lake Cahuilla Dry Periods Dates of the Two Most Recent Surface Ruptures on the Southernmost SAF Recalculated: Bulletin of the Seismological Society of America, **108**, 2634–2649, doi:10.1785/0120170392.

Rockwell. T.K., Meltzner, A.J., Haaker, E.C., and Madugo, D. (2022). The late Holocene history of Lake Cahuilla: Two thousand years of Repeated fillings within the Salton Trough, Imperial Valley, California, Quaternary Science Reviews, **282**, 107456, https://doi.org/10/1016/j.quascirev.2022.107456.

Ross, J.E. (2020). Formation of California's Salton Sea in 1905-1907 was not "accidental". In: Miller, D.M. (Ed.), Changing Facies: the 2020 Desert Symposium Field Guide and Proceedings, Desert Symposium, Inc., Zzyzx, CA, 217-230, http://www.desertsymposium.org/History.html.

Rymer, M.J. (2000). Triggered surface slips in the Coachella Valley area associated with the 1992 Joshua Tree and Landers, California, earthquakes, Bull. Seismol. Soc. Am. **90**, 832-848, https://doi.org/10.1785/0119980130.

Rymer, M.J., Boatwright, J., Seekins, L.C., Yule, J.D., and Liu, J. (2002). Triggered surface slips in the Salton Trough associated with the 1999 Hector Mine, California, earthquake, Bull. Seismol. Soc. Am. **92**, 1300-1317, https://doi.org/10.1785/0120000935.

Salisbury, J.B., Rockwell, T.K., Middleton, T.J., and Hudnut, K.W. (2012). LiDAR and Field Observations of Slip Distribution for the Most Recent Surface Ruptures along the Central San Jacinto Fault, Bulletin of the Seismological Society of America, **102**, no. 2, 598-619, doi: 10.1785/0120110068.

Salisbury, J.B., Haddad, D.E., Rockwell, T., Arrowsmith, J.R., Madugo, C., Zielke, O., and Scharer, K. (2015). Validation of meter-scale surface faulting offset measurements from high-resolution topographic data, Geosphere **11**, 1884-1901, https://doi.org/10/1130/GES01197.1.

Schwartz, D.P. and Coppersmith, K.J. (1984). Fault Behavior and Characteristic Earthquakes: Examples from the Wasatch and San Andreas Fault Zones, Journal of Geophysical Research, **89**, No. B7, 5681-5698, doi:10.1029/JB089iB07p05681.

Shimazaki, K. and Nakata, T. (1980). Time-predictable recurrence model for large earthquakes, Geophysical Research Letters, **7**, Issue 4, 279-282, doi:10.1029/GL007i004p00279.

Sieh, K.E., and Williams, P.L. (1990). Behavior of the southernmost San Andreas Fault during the past 300 years: Journal of Geophysical Research: Solid Earth, **95**, 6629–6645, doi:10.1029/JB095iB05p06629.

Tymofyeyeva, E., Fialko, Y., Jiang, J., Xu, X., Sandwell, D., Bilham, R., Rockwell, T., Blanton, C., Burkett, F., Gontz, A., and Moafipoor, S. (2019). Slow slip event on the southern San Andreas Fault triggered by the 2017 Mw 8.2 Chiapas (Mexico) earthquake, J. Geophys. Res. Solid Earth **124**, https://doi.org/10.1029/2018JB016765.

U.S. Geological Survey and California Geological Survey, Quaternary fault and fold database for the United States, accessed January 2022, at https://www.usgs.gov/natural-hazards/earthquake-hazards/faults.

Waters, M.R. (1983). Late Holocene lacustrine chronology and archaeology of ancient Lake Cahuilla, California, Quat. Res. **19**, 373-387, https://doi.org/10.1016/0033-5894.

Wei, M., Sandwell, D., Fialko, Y., and Billah, R. (2011). Slip on faults in the Imperial Valley triggered by the 4 April 2010 Mw 7.2 El Major-Cucapah earthquake revealed by InSAR, Geophys. Res. Lett. **38** (1), 1-6, L01308, https://doi.org/10.1029/2010GL045235.

Weldon, R.J., Fumal, T.E., Biasi, G.P., and Scharer, K.M. (2005). Past and future earthquakes on the San Andreas fault, Science, **308**, 966-967.

Younker, L.W., Kasameyer, P.W., and Tewhey, J.D. (1981). Geological, geophysical, and thermal characteristics of the Salton Sea geothermal field, California, Journal of Volcanology and Geothermal Research, 1-74.

Zielke, O., Arrowsmith, R.J., Ludwig, L.G., and Akciz, S.O. (2010). Slip in the 1857 and Earlier Large Earthquakes Along the Carrizo Plain, San Andreas Fault, Science, **327**, 1119-1122, doi: 10.1126/science.1182781.

Zielke, O. and Arrowsmith, R.J. (2012). LaDiCaoz and LiDARimager – MATLAB GUIs for LiDAR data handling and lateral displacement measurement, Geosphere, **8**, no. 1, 206-221, doi: 10.1130/GES00686.1.

Return to Salt Creek

After the trench at Ferrum on the flank of Durmid Hill turned out to be too shallow, and the prospect of deepening to a sufficient depth deemed infeasible, we opted to see what we could do at Salt Creek to salvage a southernmost San Andreas paleoseismic record. Fortuitously, logs, photos, trench mosaics, and some radiocarbon data that had been thought to be lost were discovered by Dr. Pat Williams. He joined our project, and we proceeded to reassess the potential to finalize that several years of work that had been completed at Salt Creek by Williams and G. Seitz. The main Salt Creek trench T1, was largely still open and intact, albeit highly degraded after 15 years of neglect. Nonetheless, the mosaic of the north face, and part of the south face, were found along with numerous annotated photographs. The Salt Creek Canyon wall was also quite accessible.

During the winter and spring of 2022, we reoccupied the Salt Creek site, collected numerous new charcoal samples, completed mosaics for the rest of trench T1, and logged most exposures. The logging was completed on the photomosaics and checked in the field to the extent possible (some exposures were quite degraded). Pat Williams worked with us in all aspects of the Salt Creek part of this project, and was invaluable for both bringing to light lost data and, perhaps as important, providing a memory or link to the legacy data such that we could complete the fieldwork and move towards publication.

We organized a trench review that included both Williams and Seitz (CGS) as well as collaborator Kate Scharer (USGS) and Phillip Greene (USGS), Tim Dawson (CGS), Ryley Hill and Matt Weingarten (SDSU) and the 2022 neotectonics class from SDSU (which provided much labor in re-clearing exposures over several field trips). This brought everyone up to date on the progress at the as well as allowed for vigorous debate on stratigraphic relations and the site chronology.

A major focus of our effort was to better define the site stratigraphy and ages of units. Towards that end, we dated 49 charcoal samples (Table 4) that advance the understanding of the site. Along with the new logging (ongoing) and age data, we are working towards integrating all data by the end of 2022. This project, to resurrect Salt Creek, turned out to be a more work than we had counted on, so it is not complete at the time of writing of this report. That said, it was beyond what we proposed in our NEHRP submission and Salt Creek will get published soon!

Table 4. *New radiocarbon dates from Salt Creek stratigraphy. Locations of all dates are located on trench logs, along with most of the previous dates analyzed for the site.*

Radiocarbon Dates for Salt Creek Trench Samples								
UCIAMS No.	Sample Location	Sample Name	Fraction Modern	±	$D^{14}C$ (‰)	±	^{14}C age (BP)	±
95089		SC1-i	0.9530	0.0042	-47.0	4.2	385	40
95090		SC1-g	0.9153	0.0041	-84.7	4.1	710	40
95091		SC1-b	0.9094	0.0040	-90.6	4.0	765	40
95092		SC1-e	0.9361	0.0034	-63.9	3.4	530	30

95093		SC1-p	0.8269	0.0037	-173.1	3.7	1525	40
95094		SC1-q	0.8857	0.0039	-114.3	3.9	975	40
98641		SC-03-L1-2	0.7011	0.0032	-298.9	3.2	2850	40
98642		SC-03-L1-3	0.8655	0.0040	-134.5	4.0	1160	40
98643		SC-03-L1-4	0.8641	0.0039	-135.9	3.9	1175	40
98644		SC-03-L1-8	0.9403	0.0043	-59.7	4.3	495	40
98645		SC-03-L1-11	0.8895	0.0037	-110.5	3.7	940	35
98646		SC-03-L3-1	0.9382	0.0043	-61.8	4.3	515	40
98647		SC-03-L3-3	0.9210	0.0042	-79.0	4.2	660	40
98648		SC-03-L3-5	0.9007	0.0041	-99.3	4.1	840	40
98649		SC-03-L3-7	0.8969	0.0046	-103.1	4.6	875	45
98650		SC-03-L3-8	0.8546	0.0032	-145.4	3.2	1260	35
106846		SC-04-1	0.9668	0.0035	-33.2	3.5	270	30
106847	Stream exp.	SC-04-2	0.9028	0.0033	-97.2	3.3	820	30
106848	Stream exp.	SC-04-3	0.8953	0.0042	-104.7	4.2	890	40
106849	Stream exp.	SC-04-4	0.8984	0.0033	-101.6	3.3	860	30
106850		SC-04-5	0.8706	0.0055	-129.4	5.5	1110	60
106851		SC-04-6	0.8658	0.0041	-134.2	4.1	1155	40
106852		SC-04-7	0.6619	0.0047	-338.1	4.7	3320	60
106853		SC-04-8	0.6630	0.0024	-337.0	2.4	3300	30
106854		SC-04-9	0.9326	0.0046	-67.4	4.6	560	40
106877		SC-04-1fu	0.9511	0.0049	-48.9	4.9	405	45
126289		SC-2-06	0.5916	0.0023	-408.4	2.3	4215	35

126290		SC-5-06	0.5926	0.0023	-407.4	2.3	4205	35
126291		SC-6-06	0.6139	0.0024	-386.1	2.4	3920	35
126292		SC-13-06	0.6016	0.0023	-398.4	2.3	4080	35
126293		SC-20-06	0.8606	0.0033	-139.4	3.3	1205	35
126294	South Wall	SC-21-06	0.5921	0.0023	-407.9	2.3	4210	35
126295	South Wall	SC-23-06	0.6612	0.0026	-338.8	2.6	3325	35
126296	South Wall	SC-27-06	0.0020	0.0005	-998.0	0.5	50100	2200
126297	South Wall	SC-29-06	0.0025	0.0005	-997.5	0.5	48200	1700
126313	Stream exp.	SC-39-06	0.8132	0.0029	-186.8	2.9	1660	30
126298	Stream exp.	SC-40-06	0.8818	0.0034	-118.2	3.4	1010	35
126299	Stream exp.	SC-41-06	0.9034	0.0035	-96.6	3.5	815	35
126300	Stream exp.	SC-42-06	0.9540	0.0035	-46.0	3.5	380	30
126301	Stream exp.	SC-43-06	0.9558	0.0041	-44.2	4.1	365	35
126314	Stream exp.	SC-43sh-06	0.8389	0.0033	-161.1	3.3	1410	35
126302	Stream exp.	SC-44-06	0.7457	0.0026	-254.3	2.6	2355	30
126303		SC-45-06	0.2616	0.0050	-738.4	5.0	10770	160
126304		SC-46-06	0.6303	0.0025	-369.7	2.5	3705	35
255771	North Wall	SC-1N-05	0.6755	0.0011	-324.5	1.1	3150	15
255772	North Wall	SC-2N-05	0.6611	0.0011	-338.9	1.1	3325	15
255773	South Wall	SC-3S-05	0.0001	0.0006	-999.9	0.6	>53400	N/A
255774	South Wall	SC-4S-05	0.5451	0.0009	-454.9	0.9	4875	15
255775	South Wall	SC-5S-05	0.6527	0.0031	-347.3	3.1	3430	40
255776	South Wall	SC-7S-05	0.6755	0.0011	-324.5	1.1	3150	15

255777	North Wall	SC-8N-05	0.6084	0.0010	-391.6	1.0	3990	15
255778	South Wall	SC-12S-05	0.5731	0.0009	-426.9	0.9	4470	15
255779	North Wall	SC-15N-05	0.6667	0.0011	-333.3	1.1	3255	15
255780	North Wall	SC-16N-05	0.6800	0.0014	-320.0	1.4	3100	20
255781	North Wall	SC-17N-05	0.6586	0.0013	-341.4	1.3	3355	20
255782	South Wall	SC-19S-05	0.6744	0.0012	-325.6	1.2	3165	15
255783	South Wall	SC-25S-05	0.8935	0.0014	-106.5	1.4	905	15
255817	South Wall	SC-21S-05	1.0774	0.0018	77.4	1.8	MODERN	N/A
257977	South Wall	SC-22-C23	0.8951	0.0017	-104.9	1.7	890	20
257970	Stream exp.	SC-22-C3	0.9016	0.0016	-98.4	1.6	830	15
257976	South Wall	SC-22-C21	0.7051	0.0015	-294.9	1.5	2805	20
257971	Stream exp.	SC-22-C12	0.9191	0.0016	-80.9	1.6	680	15
257973	Stream exp.	SC-22-C14	0.9177	0.0016	-82.3	1.6	690	15
257975	South Wall	SC-22-C18	0.6802	0.0012	-319.8	1.2	3095	15
257972	Stream exp.	SC-22-C13	0.8897	0.0015	-110.3	1.5	940	15
257969	Stream exp.	SC-22-C1	0.8945	0.0017	-105.5	1.7	895	20
257974	Stream exp.	SC-22-C16	0.8945	0.0015	-105.5	1.5	895	15
257978	North Wall	SC-22-C28	0.6826	0.0011	-317.4	1.1	3065	15
259827	South Wall	SC-22-C59	0.8947	0.0015	-105.3	1.5	895	15
259828	South Wall	SC-22-C60	0.8960	0.0015	-104.0	1.5	880	15
259829	South Wall	SC-22-C61	0.8943	0.0019	-105.7	1.9	900	20
259830	South Wall	SC-22-C63	0.5438	0.0011	-456.2	1.1	4895	20
259831	South Wall	SC-22-C66	0.5552	0.0011	-444.8	1.1	4725	20

259832	North Wall	SC-22-C70	0.8914	0.0017	-108.6	1.7	925	20
259833	South Wall	SC-22-C71	0.5656	0.0014	-434.4	1.4	4575	20
259834	South Wall	SC-22-C72	0.5793	0.0027	-420.7	2.7	4385	40
259835	South Wall	SC-22-C73	0.5479	0.0010	-452.1	1.0	4835	15
259836	Stream exp.	SC-22-C74	0.6692	0.0013	-330.8	1.3	3225	20
259837	Stream exp.	SC-22-C75	0.8897	0.0017	-110.3	1.7	940	20
259838	Stream exp.	SC-22-C78	0.8898	0.0016	-110.2	1.6	940	15
259839	Stream exp.	SC-22-C79	0.9056	0.0016	-94.4	1.6	795	15
263010	North Wall	SC-22-C85	0.3147	0.0016	-685.3	1.6	9285	45
263011	North Wall	SC-22-C88	0.7552	0.0012	-244.8	1.2	2255	15
263012	North Wall	SC-22-C91	0.9276	0.0015	-72.4	1.5	605	15
263013	North Wall	SC-22-C93	0.6644	0.0012	-335.6	1.2	3285	15
263014	North Wall	SC-22-C94	0.6704	0.0010	-329.6	1.0	3210	15
263015	North Wall	SC-22-C95	0.0486	0.0077	-951.4	7.7	24300	1300
263016	North Wall	SC-22-C97	1.0716	0.0018	71.6	1.8	Modern	
263017	North Wall	SC-22-C99	0.6734	0.0012	-326.6	1.2	3175	15
263018	North Wall	SC-22-C100	0.6623	0.0011	-337.7	1.1	3310	15
263019	South Wall	SC-22-C101	0.5567	0.0023	-443.3	2.3	4705	35
263020	South Wall	SC-22-C103	0.6788	0.0011	-321.2	1.1	3110	15
263021	North Wall	SC-22-C106	0.8960	0.0015	-104.0	1.5	880	15